A UNITED STATES
DEPARTMENT OF
COMMERCE
PUBLICATION

ESSA Technical Memorandum ERLTM-ARL 20

U.S. DEPARTMENT OF COMMERCE
ENVIRONMENTAL SCIENCE SERVICES ADMINISTRATION
Research Laboratories

Atmospheric Transport and Diffusion

in the Planetary Boundary Layer

Air Resources
Laboratories
SILVER SPRING,
MARYLAND
June 1970

ESSA RESEARCH LABORATORIES

AIR RESOURCES LABORATORIES

IMPORTANT NOTICE

U.S. DEPARTMENT OF COMMERCE
Environmental Science Services Administration
Research Laboratories

ESSA Technical Memorandum ERLTM-ARL 20

ATMOSPHERIC TRANSPORT AND DIFFUSION
IN THE PLANETARY BOUNDARY LAYER

I. Van der Hoven, Editor

Contributors

J. K. Angell	C. R. Dickson	D. H. Slade
A. B. Bernstein	E. H. Markee	G. E. Start
D. J. Bjorem	D. H. Pack	L. L. Wendell

Semiannual Research Program Review
July - December 1969
U. S. Atomic Energy Commission

Air Resources Laboratories
Silver Spring, Maryland
June 1970

PREFACE

    In accordance with the letter of agreement of July 24, 1969, with the
U. S. Atomic Energy Commission, Division of Reactor Development and
Technology, Environmental and Sanitary Engineering Branch, the Air Resources
Laboratories have continued their study of atmospheric transport and
diffusion in the planetary boundary layer, micrometeorology, diffusion
climatology, and the application of this work to the disposal of radioactive
waste gases into the atmosphere. The research is technically administered
and supervised through the Air Resources Environmental Laboratory of the
Air Resources Laboratories. The work is performed at the Air Resources
Laboratories Headquarters in Silver Spring, Maryland, and at the Air
Resources Idaho Falls Laboratory, National Reactor Testing Station, Idaho.
Any inquiry on the research being performed should be directed to the
editor, Isaac Van der Hoven, Chief, Air Resources Environmental Laboratory,
Air Resources Laboratories, Environmental Science Services Administration,
8060 - 13th Street, Silver Spring, Maryland 20910.

TABLE OF CONTENTS

ATMOSPHERIC TRANSPORT AND DIFFUSION
IN THE PLANETARY BOUNDARY LAYER

AIR RESOURCES LABORATORIES SEMIANNUAL RESEARCH PROGRAM REVIEW
FOR THE ENVIRONMENTAL AND SANITARY ENGINEERING BRANCH
DIVISION OF REACTOR DEVELOPMENT AND TECHNOLOGY
U. S. ATOMIC ENERGY COMMISSION

JULY - DECEMBER 1969

1. RESEARCH AT AIR RESOURCES LABORATORIES HEADQUARTERS, SILVER SPRING, MD.

1.1 Mesoscale Lagrangian Studies (Tetroon Research)

This is a joint research effort of several of the Air Resources Laboratories
with the sponsorship of both the Atomic Energy Commission (AEC) and the
National Air Pollution Control Administration (NAPCA).

1.1.1 Lagrangian-Eulerian Relationships

The Lagrangian-Eulerian scale ratios derived from tetroon flights past
the BREN tower at the Nevada Test Site have been criticized on the basis of
tetroon response to vertical air motion. With the assumption of a sinusoidal
vertical-velocity variation, it has been shown theoretically from consideration
of the forces acting on the tetroon that the difference between air parcel
and tetroon vertical velocity is proportional to tetroon period of vertical
oscillation and inversely proportional to the vertical air velocity.
Accordingly, as the period of tetroon oscillation in the vertical increases,
the tetroon-derived vertical velocity variance becomes more and more an
underestimate of the Lagrangian-Eulerian scale ratio. The attempt is now
being made to "correct" the tetroon-derived vertical velocity spectra
according to the ratio of period of vertical oscillation to vertical air
velocity. The individual flight spectra are also being composited to ensure
greater reliability of the scale estimates.

1.1.2 Urban Wind Structure Studies - Columbus, Ohio

The analysis and preliminary write-up of the Columbus experiment has been
completed. The nighttime tetroon flights at heights of 100 - 200 m indicate
ascending air motion upwind and descending air motion downwind of the city in
relatively unstable atmospheres, but no appreciable vertical air motion in
stable atmospheres. The descending motion extends downwind and laterally from
city center in the manner of a bow wave from a ship and appears to occur
further downwind with increase in height.

At these heights the decrease in wind speed across the city at night averages 0.4 m/sec or 4 percent of the geostrophic speed, but varies from 40 percent for a flight directly over downtown in relatively unstable conditions to negligible speed change under stable conditions. The city induces an anticyclonic wind turning of about 3° under most stability conditions, with a marked increase in this turning as the night progresses, probably a result of the heat island effect and the barrier effect dominating the frictional effect. In relatively unstable atmospheres the city acts as a barrier to the airflow at these heights, the flights to the left of city center (looking downwind) having a slight cyclonic and flights to the right of city center a quite strong anticyclonic curvature. This effect is indicated in figure 1, where the lateral scale is exaggerated 4 times relative to the longitudinal scale. Because of this swerving away from downtown, the tetroon trajectories when plotted in the transverse plane show evidence of counter-rotating helices either side of downtown.

An increase in nighttime turbulence intensity, which is twice as high for the vertical component, is noted only for flights directly over downtown in relatively unstable atmospheres. The tetroon-derived stress increases by 0.4 dynes/cm² in the mean as the balloons cross the city, but the relation of this stress to the Reynolds stress in problematical.

In summary, useful information concerning urban influences on the air flow can be obtained from tetroon flights and this information would be even more valuable if simultaneous flights could be made.

1.1.3 Use of Pressure Data to Derive Wind Data

The possibility of using observations of pressure to calculate the geostrophic wind is an attractive one since data from such observations are numerous, routinely reported every hour, and less subject to vary with location of the barometer. Wind data derived from tetroon flights have been compared with geostrophic winds determined from hourly surface pressure data based on pressures from two different data sets (four stations each) to examine the effect of station spacing. One set of stations has a mean separation distance of 364 km, the other 266 km. Both sea level pressure and "station" pressure values were used, the latter referenced to a common height for each pair of stations through a height correction based on the NACA Standard Atmosphere. The purpose of these differing data bases is to examine the differences created by the reduction to sea level correction.

In addition to the graphical technique for calculating the geostrophic wind, a program was prepared for an electronic desk calculator that incorporates all the various constants, conversion factors, etc., whereby the operator simply can enter the observed pressures in a specified order to obtain the geostrophic wind direction and speed in degrees and meters per second.
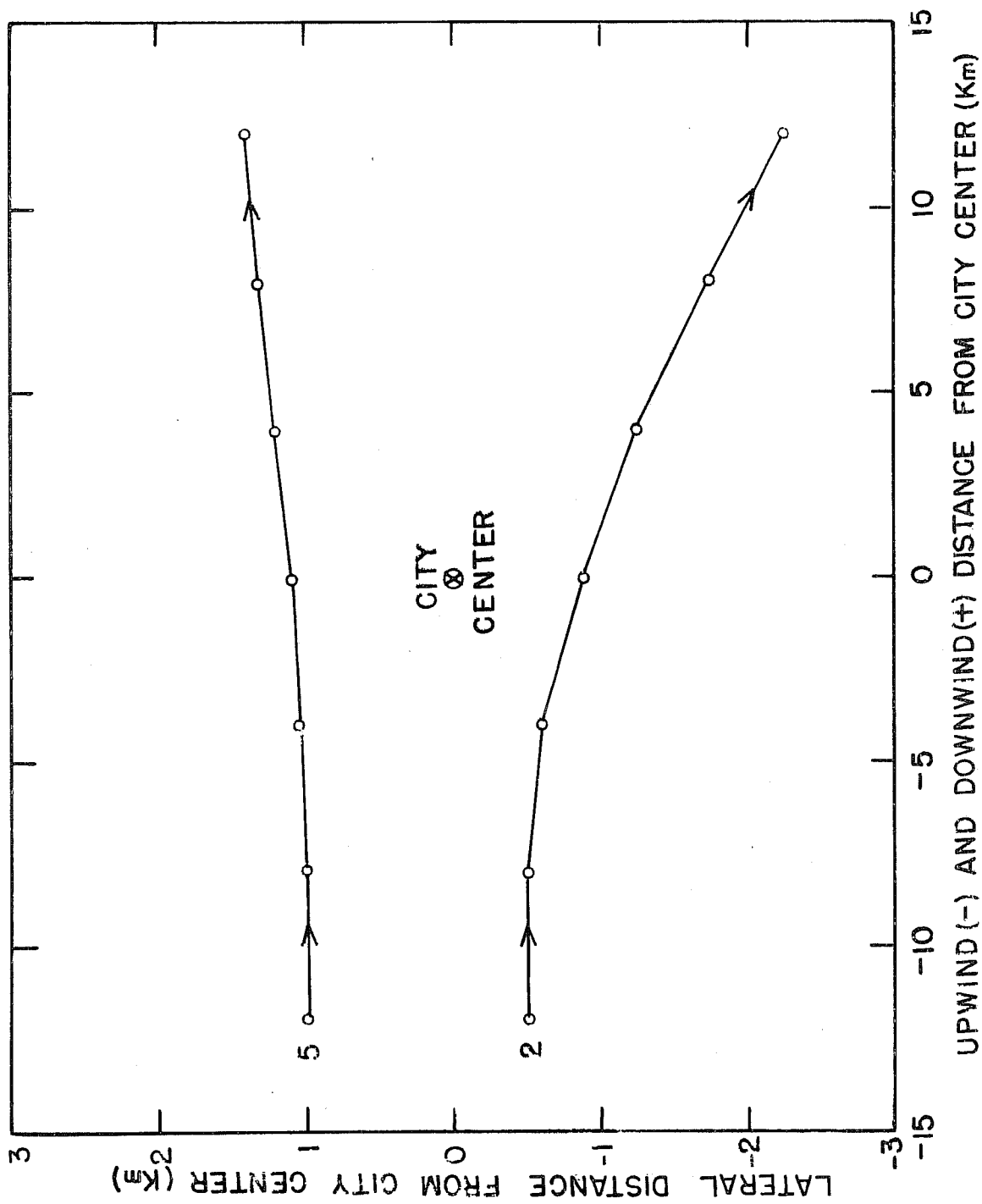
2

Figure 1. Horizontal projection of mean nighttime tetroon trajectories either side of downtown Columbus, Ohio, for flights in relatively unstable atmospheres. The number of trajectories making up the mean is indicated at left. The lateral scale is exaggerated 4 times relative to the longitudinal scale.

Preliminary indications are that these calculated geostrophic winds, now being analyzed, are systematically related to the winds observed with tetroons. Figure 2 shows the difference in mean direction and mean speed between calculated geostrophic wind and the tetroon observations. Also shown are three theoretical versions of these differences derived from the so-called Ekman spiral (S after Sutton and B-1 and B-2 after Bergeron). Each of these used slightly different assumptions and initial values. A fourth computation by Haurwitz (H), for a very deep mixed layer typical of daytime convection, but not of the conditions prevailing at night over Columbus, is shown for the direction difference but not for speed since his assumed geostrophic speed of 20 m/sec is much larger than shown by our data. The plotted point at 450 m is not likely to be significant since it is only a mean of all the observations between 250 and 700 and represents far too few observations to be reliably applied to this deep a layer. The wind direction differences between the tetroon-derived data and the geostrophic winds vary as a function of height of the wind observation; the largest differences (about 60°) are at the lowest level of 50 m above the ground and the smallest (about 20°) 250 m above the ground. The sense of the difference is for the observed wind to be to the left (indraft) of that calculated, as would be expected from frictional effects. Observed wind speeds are also less near the ground, becoming very nearly the same as the calculated geostrophic values above 250 m. Since the theoretical curves are based on a constant vertical eddy exchange coefficient, and since the real, observed winds are influenced by forces not included in the theoretical treatment (vertical thermal gradients, inertial accelerations, etc.), the agreement is probably better than one would expect.

In computing geostrophic winds we find that the larger grid size gives better comparisons than the 266-km grid. This is attributed to the limitations of accuracy in the present observing system, which permits pressure resolution to 0.005 inches of mercury (0.17 mb) and a possible error due to "rounding" of ≠ .005 inches. These resolution and error values become increasingly significant as the spacing between observing stations is decreased, especially for small pressure gradients. The data will also be examined for the effects of thermal stability as measured by helicopter soundings.

1.1.4 Urban Wind and Air Pollution Studies - Los Angeles

A major field program to measure the three-dimensional trajectories and associated air quality with tetroons, radar, and an instrumented helicopter was carried out in September and early October. A considerable logistics effort to effect radar emplacement, acquisition of commercial power, radio communications, and helicopter instrumentation was completed by the Idaho Falls Field Research Office (FRO) and the Atmospheric Physics and Chemistry Laboratory. Assistance was received from various municipal agencies in the Los Angeles Basin, especially from all offices of the City of Glendale and from many police departments.

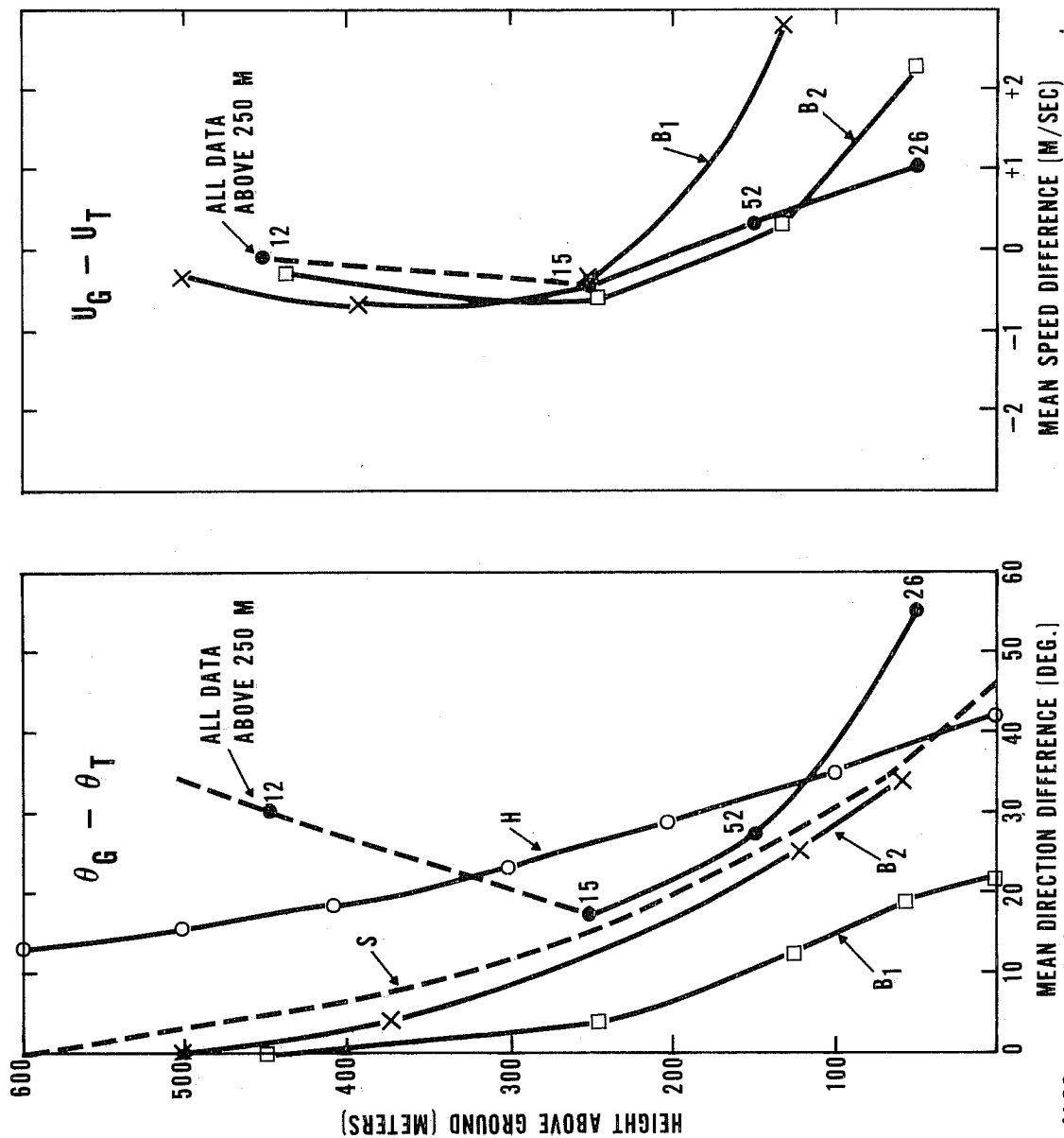Figure 2. Mean differences between calculated geostrophic and tetroon wind direction and speed. Positive values for direction indicate tetroon flow counterclockwise from geostrophic direction and geostrophic speeds higher than tetroon speeds. Numbers adjacent to plotted points are the number of comparisons at each height. Several theoretical Ekman spirals are shown (S—Sutton, B-1, B2—Bergeron, H—Haurwitz).

The radar was installed at 2500 ft MSL on Mt. Thom north of Glendale. Since tetroon flight levels are generally low, an elevated site was mandatory if coverage of a majority of the Basin from ocean to foothills was to be achieved, and it also facilitated essential radio communication between the helicopter and the launch site.

A total of 105 tetroon flights were made from a variety of launch sites in the Basin; 70 hours of helicopter observations were obtained simultaneously. For the first 47 flights the data acquisition rate was at 10-sec intervals. This rate was increased to once per second for range, elevation, and azimuth information for the last 58 flights. The average length of the flights was about 3 or 4 hours, but a few tetroons were airborne for more than 10 hours, with the longest one tracked for $18\frac{1}{2}$ hours. Since each hour of radar data produced 14,400 information items (including time identification), data editing and processing presented a problem that could only be met by the FRO data logging system and computer processing. Preliminary review of the data indicate that the 1-sec data rate is an advantage over the 10-sec values in producing more stable 1-min average wind components.

In the quantitative processing of the data, which is continuing, four situations of particular interest have been identified. The first was the progressively deeper penetration of the westerly sea breeze as the day progressed. Launches from Redondo Beach as shown in figure 3 (flights 18, 19, and 30) indicate a shift to a south or southwest sea breeze after an initial eastward trajectory. These data suggest that air arriving near Azusa after about 1 P.M. did not acquire its pollutant burden from the center city area.

Second, one tetroon was launched to try to have its flight coincide with the leading edge of the sea breeze and it apparently did so. The trajectory is shown in figure 4 as flight No. 96 released from launch site "B" at 1206 on September 30, 1969, and tracked for approximately 4 hours. During this time, the most vigorous vertical motion and maximum turbulence was experienced by the helicopter. Measurements of both relative humidity and oxidant from the helicopter fluctuated rapidly over wide ranges in a logical pairing (low humidity + high oxidant; high humidity + low oxidant) in the vicinity of the tetroon.

Third, one nighttime trajectory (fig. 4, flight No. 36 released from launch site "B" at 0133 on September 17, 1969) moving slowly east-northeast along the foothills reached a "stagnation" point, where the slope drainage into the Los Angeles Basin from the northeast just balanced the opposing flow, and the balloon remained within a radius of about a mile for more than 9 hours.

Fourth, tetroon flights originating in the city-center area near sunrise as shown in figure 5 depict the high degree of stagnation over central Los Angeles that persists till midmorning, when the slope heating creates a movement north and northeast into the Glendale-Pasadena area. The resulting trajectories and timing of the first significant movement of the polluted air mass away from the downtown area were nearly identical on three separate days.
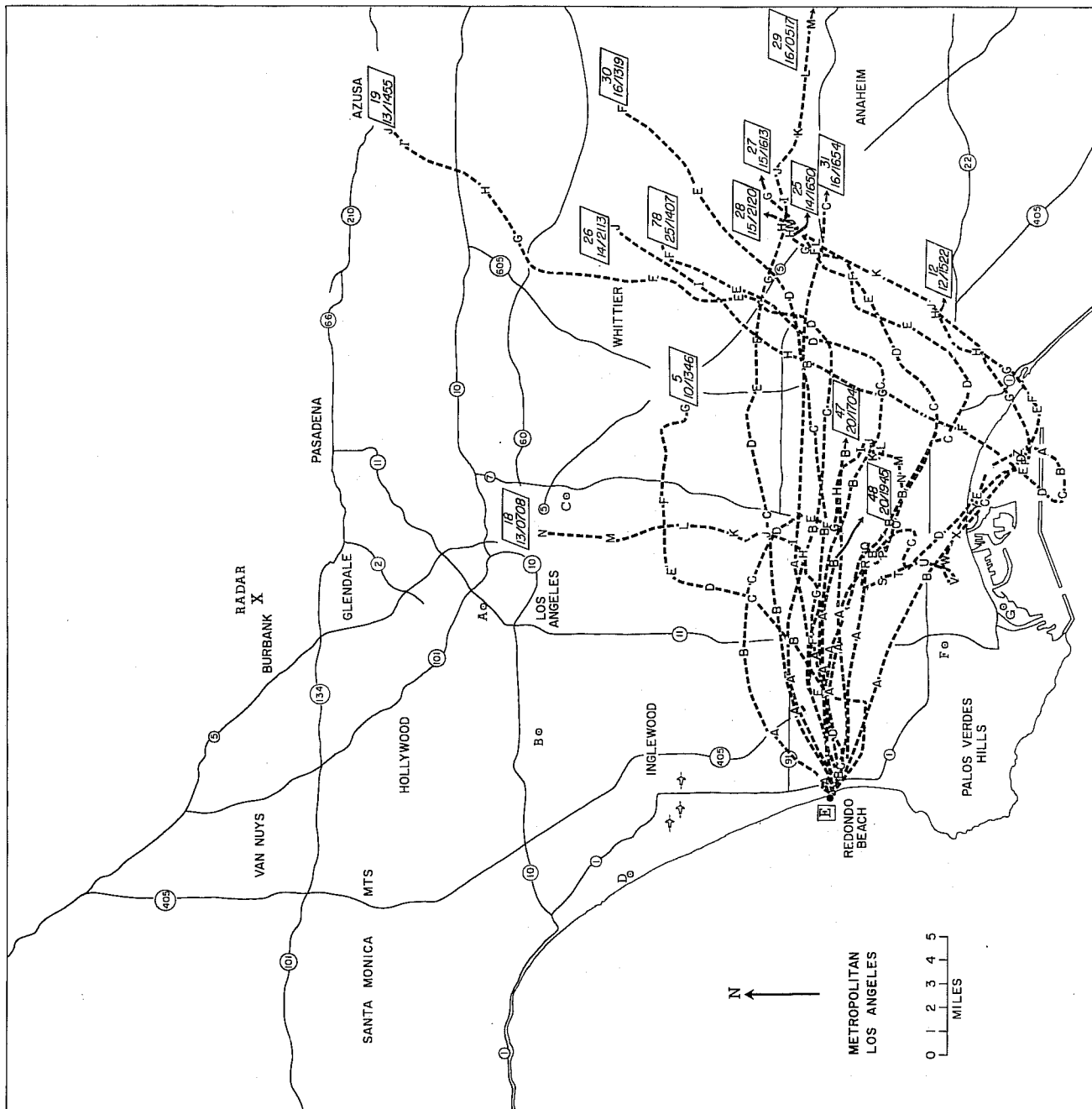
6

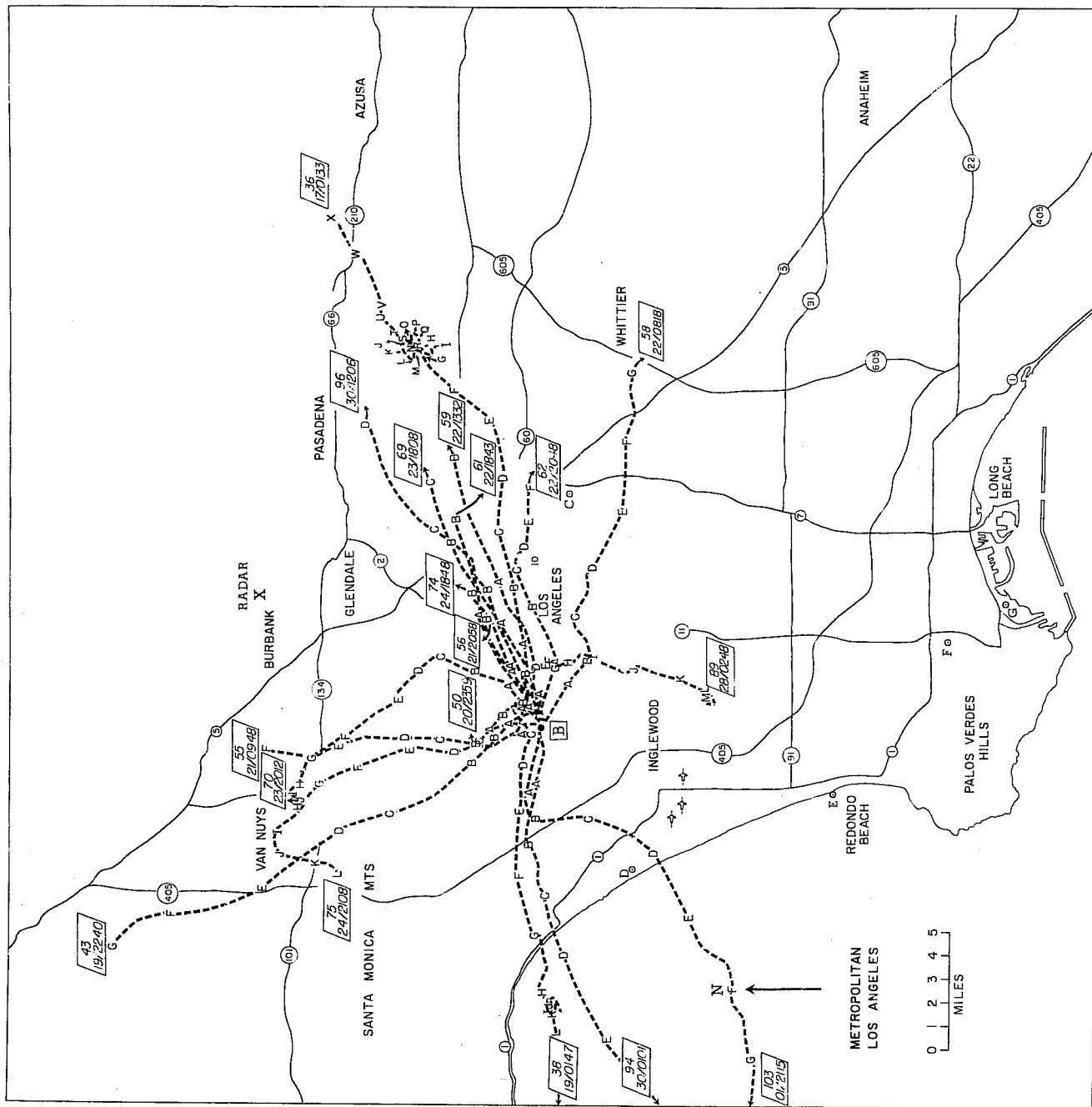Figure 3. Trajectories of tetroons launched from Redondo Beach.

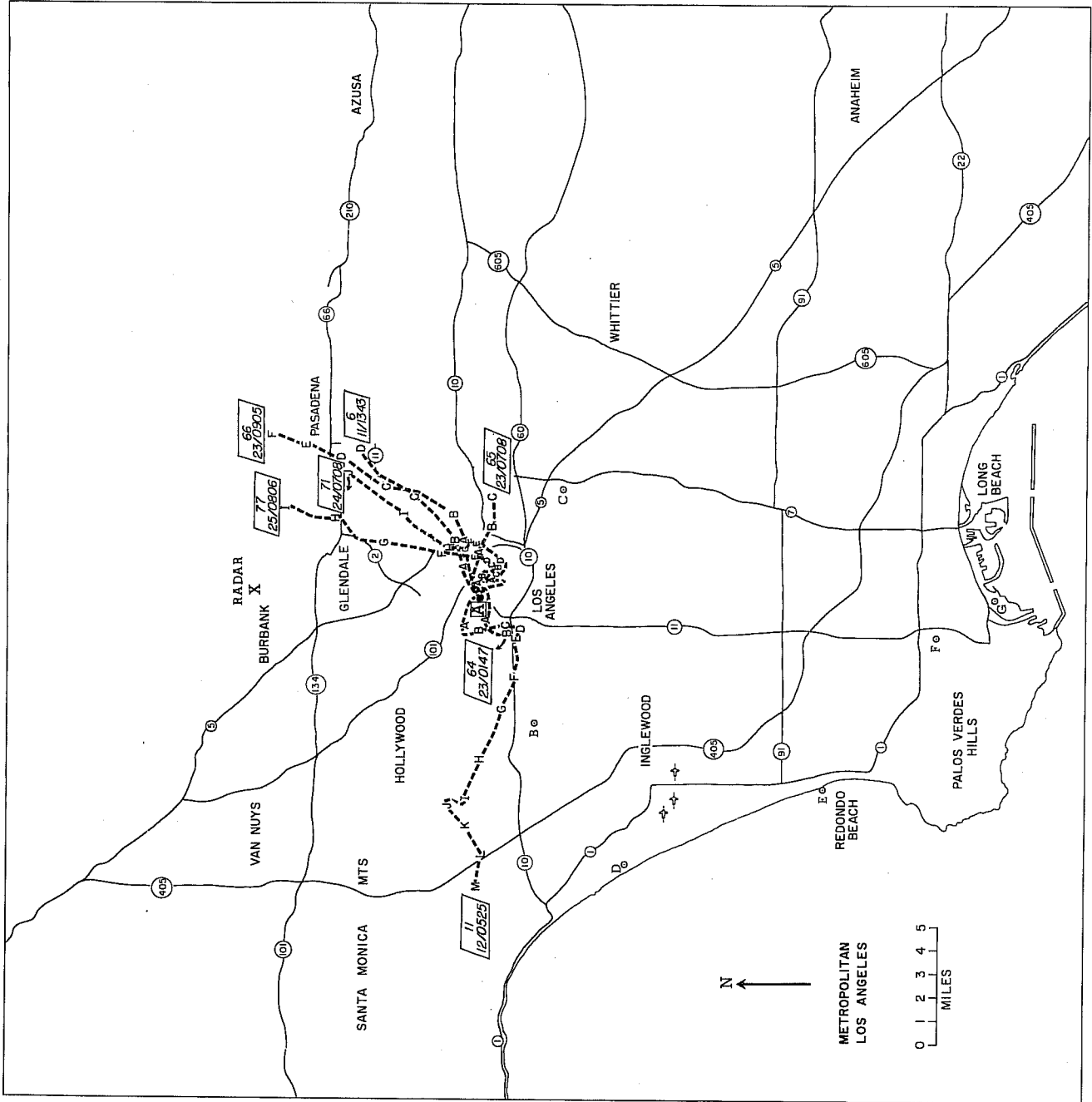Figure 4. Trajectories of tetroons launched from the Culver City area.

8

Figure 5. Trajectories of tetroons launched from Los Angeles city area.

9

One of the objectives of the experiments was to acquire air quality data along the trajectory of an "air parcel" as it was represented (approximately) by the three-dimensional path of the tetroon. This required vectoring the helicopter to the vicinity of the tetroon usually under conditions of greatly restricted visibility. It was gratifying to find that the radar controller-helicopter pilot/observer team could acquire the tetroon visually in less than 5 min of search time. The technique consisted of pre-experiment preparation of a detailed street map of the Los Angeles Basin on a scale that matched the radar plot board. Position coordinates were relayed in terms of bearings from major street intersections and landmarks (e.g., City Hall, Dodger Stadium, etc.) and further refined to within 50 yards by specifying street intersections. The critical item was tetroon height and direction of vertical motion. This latter was particularly important during afternoon flights when the tetroon vertical motions often exceeded the climb rate of the helicopter.

The air quality and meteorological data obtained by the helicopter were recorded on charts and must be manually reduced; hence this information is slow to emerge. However, figure 6 shows information along the trajectories of two different flights. On flight No. 66 released at 0905 from the city-center area the air quality oxidant readings increased from 5 parts per hundred million by volume (pphmv) during the first hour to 14 pphmv at the end of the second hour and finally to 20 pphmv at the end of the flight near Pasadena. The immediately following flight No. 67 from launch site "C" showed similar oxidant readings toward the end of the flight near Azusa. A vertical cross section of the air quality profile is shown in figure 7. The oxidant plus the NO readings are based on a chromium trioxide filter that converts $NO \rightarrow NO_2$. The NO_2 is then counted as an oxidant in the neutral KI sensor. The CHEMI-LU curve is an air quality measurement by a chemical luminescent technique. At the point of measurement over the Flood Control Basin near Azusa, the oxidant profile increased from about 26 pphmv at the surface to a peak of about 30 pphmv at an elevation of 1600 ft MSL, or 1000 ft above the ground. This seems to indicate that pollutants from the central portion of the basin concentrate at the base of the marine inversion and that presumably, as the air approaches the foothills, these high concentrations affect the surface as the terrain rises to 1600 ft MSL. It is obvious from the temperature profile shown in figure 6 that the air is relatively moist and unstable in the lower 500 ft above the ground, which explains the relatively low oxidant measurements in this layer.

1.2 Prediction of Wind Fields by Statistical Techniques

A new concept and methodology for predicting a meteorological variable by statistical techniques has been developed by Mr. G. Brier, Chief, ARL Meteorological Statistics Group. The method is being applied to the prediction of surface winds at the NRTS. The data bank was supplied by the Idaho Falls FRO meso-wind system. The basic data are the u-v wind component fields derived from the observed winds through the objective analysis technique developed at the FRO. These derived fields, rather than the basic

10
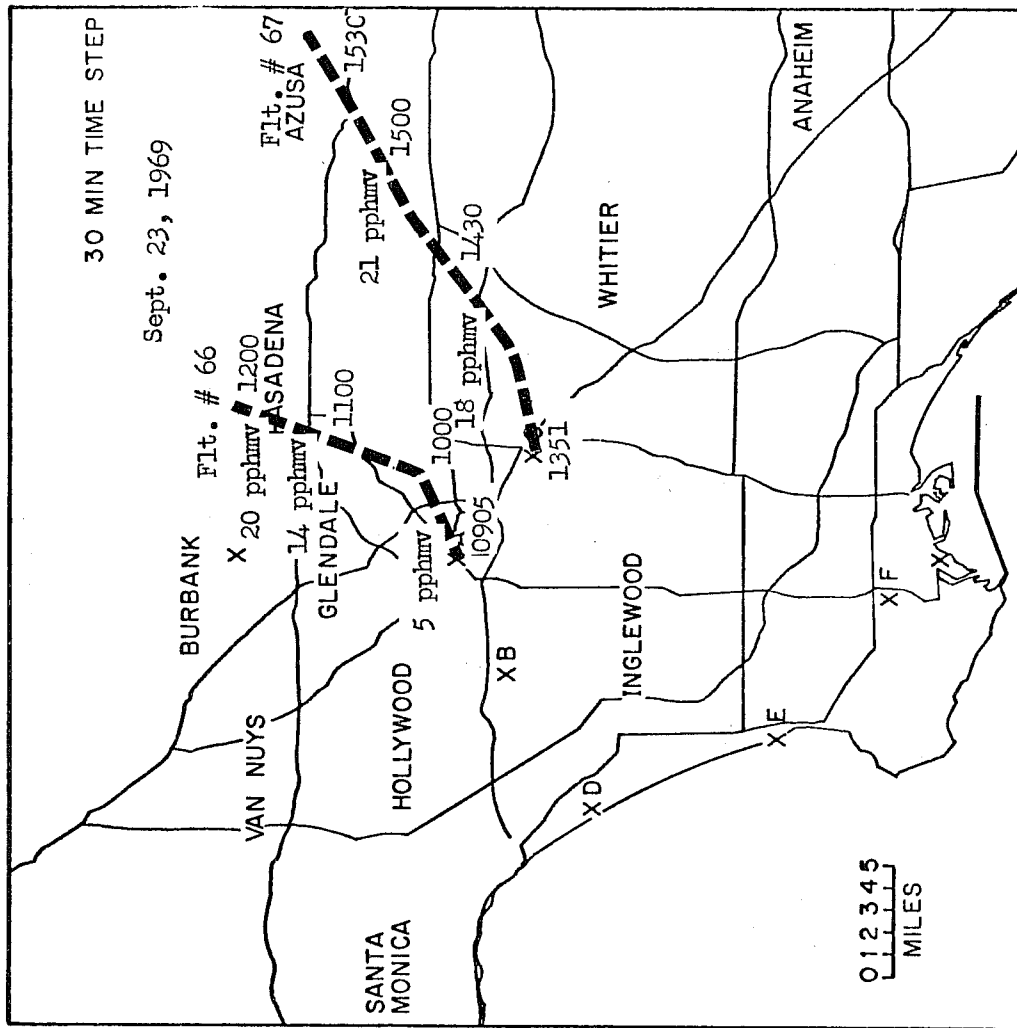
METROPOLITAN LOS ANGELES

Figure 6. Tetroon trajectories and simultaneous air
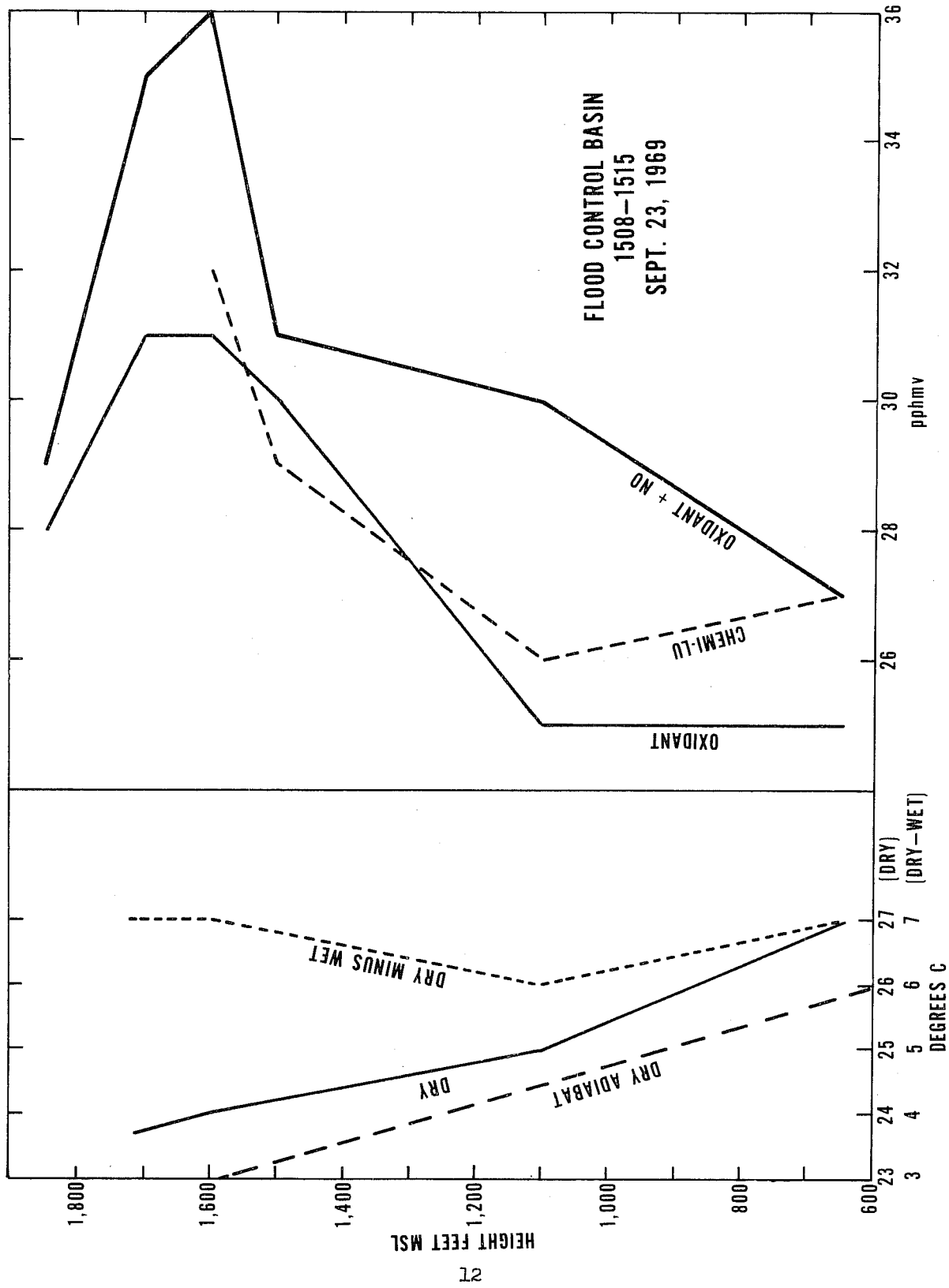quality measurements at flight altitude.

Figure 7. Air quality vertical profile over the Flood Control Basin near Azusa on September 23, 1969, between 1508-1515 h.

data, were used to avoid the complication introduced by the incomplete original wind records. The ability to predict winds 1, 6, 12, and 24 hours in advance by this method will be tested.

1.3 Mixing Length Hypotheses

In Prandtl's mixing length hypothesis the "level of origin" of a fluid particle is defined as the level at which the particle last had zero vertical velocity. Since at this level the particle is assumed to be in complete equilibrium with its environment, there is no difference between its velocity and temperature and the mean velocity and temperature at that level. Priestley and Swinbank (1947) have pointed out that this assumption may not be valid; they too define the level of origin as the level at which the particle's vertical velocity last vanished, but they permit velocity and temperature anomalies to be present. They then suggest that in momentum transfer there will be no correlation between the u anomaly of the particle at the level of origin and its w value a short time later, whereas in heat transfer the tendency for particles that are warmer than their environment to rise will result in a positive correlation between the T anomaly at the level of origin and the vertical velocity shortly thereafter. As a consequence there is a difference between K_M and K_H, the exchange coefficient for heat being larger than that for momentum under unstable conditions and smaller under stable ones.

Some evidence concerning the validity of these assumptions has been obtained by examining several series of rapid-response measurements of velocity and temperature at a fixed point. For each run, a data subset, consisting of those observations for which the vertical velocity was very close to zero, was examined. If the Prandtl assumption were correct, this subset should be characterized by velocity and temperature distributions concentrated around their mean values; the data suggest, however, that the distributions of u and T for the subset are very similar to those that apply to the entire run. If Priestley and Swinbank were correct in suggesting that, while the temperature anomaly at the level of origin contributed to the heat flux, the corresponding velocity anomaly makes no contribution to the momentum flux, then the correlation between u and T determined from the subset should be small. This appears to be the case; however, u and T tend to be correlated because both are functions of height, and this must be taken into account in deciding whether the subset correlation is sufficiently small. Since the correlation between u and T associated with their height dependence changes sign with a change from unstable to stable conditions, this question can best be looked into by examing both conditions. Thus far three runs, all representing unstable conditions, have been examined; the investigation is continuing.

13

1.4   Urban Wind Measurements on a Tall Tower - New York City

Representative wind speed data for a city are rarely obtained. An apparently high-quality, slow-speed, analog record from an instrument mounted 590 ft above ground level in lower Manhattan in New York City was obtained and offered the possibility of making approximate estimates of lateral turbulence.

The instrument was mounted on a 90-ft mast projecting from the center of a 500-ft building measuring about 100 ft on a side at the top.   The building (see fig. 8) is on the west side of Manhattan, a few hundred feet from the bank of the Hudson River.

The location of the building suggested an interesting comparison of the difference in the characteristics of the wind arriving from different sectors. Three such sectors were defined and studied. The first extended from north through east to just west of south. Air arriving from this sector travelled over or through what is probably the greatest concentration of tall buildings in any city.

A second sector extending toward the southwest was chosen. Air arriving from this sector travelled over 5 to 7 mi of water. A third sector extended westward to New Jersey. In all directions in this sector overwater travel was less than $1\frac{1}{2}$ mi.

Data from the wind recording were extracted for the following categories:

Seasons: Summer (part of June, all of July and August).
          Winter (January, February, and part of March).

Times   : For each season, data (not including light and variable wind speed and direction) were chosen for 0000 - 0100 EST, 1300 - 1400 EST and for the period $1\frac{1}{2}$ to $\frac{1}{2}$ hours before sunset.

The raw data consisted of the 60-min wind direction range, the average of the three alternate 10-min direction ranges for the hour, average hourly wind direction, and average hourly wind speed.

The standard deviation of the wind direction distribution, σ_θ , was estimated by dividing the range values by 6.0. The standard deviation of the lateral wind component was estimated from

$$\sigma_V = \sigma_\theta \, V,$$

where V is the average hourly wind speed. Such estimates have been used previously, most recently by Slade (1969).
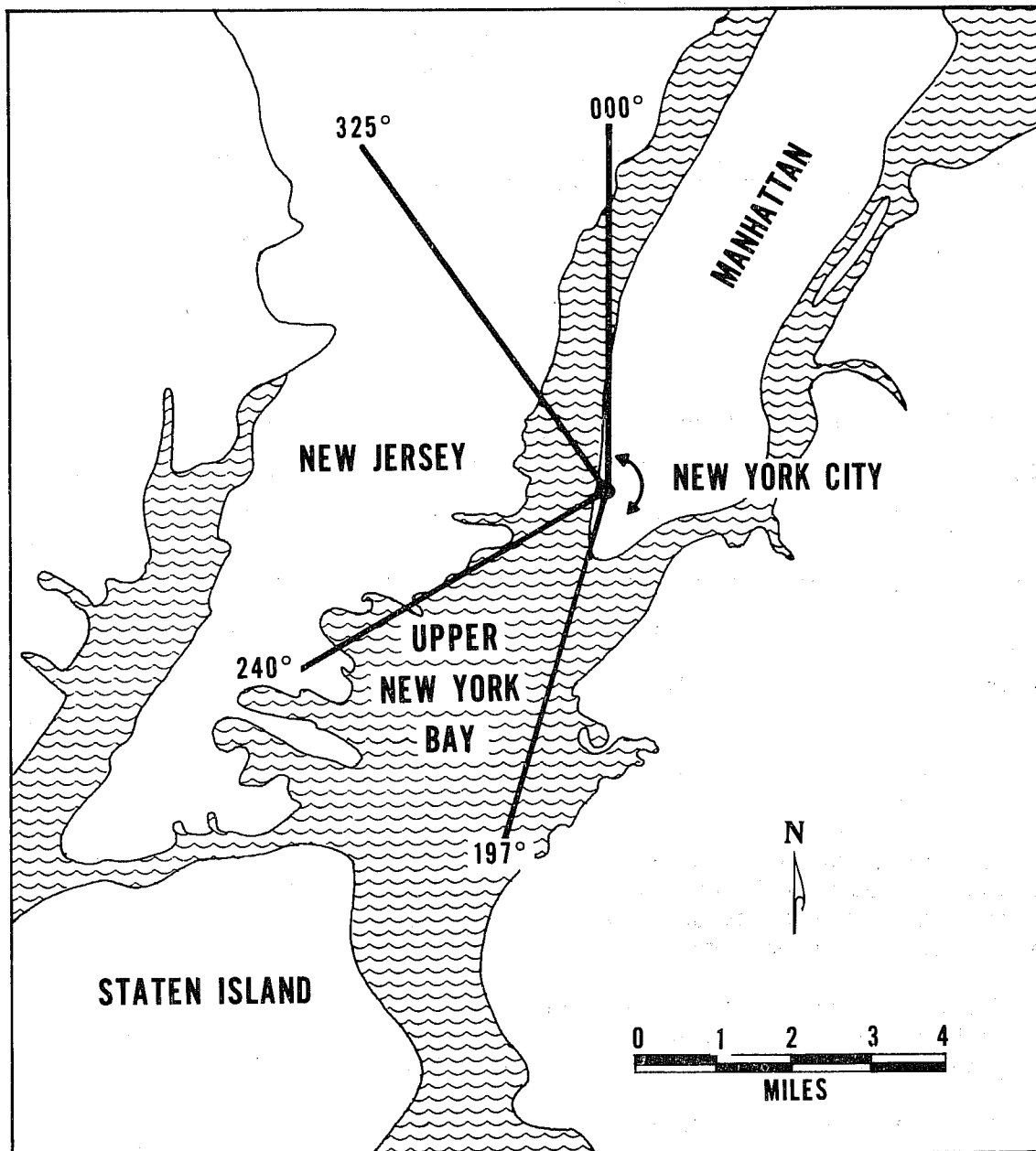
Figure 8. Geographical location of wind tower in New York City.

The ratio

$$R = \frac{\sigma_v^2(60 \text{ min}) - \sigma_v^2(10 \text{ min})}{\sigma_v^2(10 \text{ min})}$$

was calculated to give an estimate of the relative magnitude of the variance caused by long-and short-period fluctuations.

The average values of σ_θ, σ_v, R and V over all times and seasons are given in table 1.

Table 1. Data Averages for all Season and Time of Day Groups.

Direction From	σ_θ (deg)	σ_v (m/s)	R	V(m/s)
City	18.1	1.72	1.20	5.9
New Jersey	10.7	1.34	1.69	7.5
Bay	8.4	0.84	1.97	6.4

The progression of values of σ_θ, σ_v, and R from the turbulent city flow to the smooth overwater flow for these total averages is reflected in the averages for each season and time of day group as shown in table 2, where N is the number of observations.

Wind was recorded on a few occasions in the direction sector $326^\circ - 356^\circ$. Air arriving from this direction had traveled over $1\frac{1}{2} - 3$ mi of water and exhibited characteristics similar to that of the bay flow.

Many deductions of the average and turbulent characteristics of the wind over a city can be made only from fixed wind sensors. Accepting the difficulties and limitations inherent in locating such systems in an urban area, it is obvious that such instrumentation must play an essential role in any measurement program to probe the atmospheric environment of a city.

Table 2. Data Averages by Season and Time of Day

	City	New Jersey	Bay
	0000 – 0100 EST,Winter		
$\sigma_{\widetilde{\theta}}(60)$ (deg)	13.0	9.2	5.0
V (m/s)	7.5	7.7	7.2
$\sigma_{\widetilde{v}}(60)$ (m/s)	1.66	1.23	0.71
$\sigma_{\widetilde{v}}(10)$ (m/s)	1.20	0.84	0.52
R	1.08	1.27	1.32
N	12	24	12
	0000 – 0100 EST, Summer		
$\sigma_{\widetilde{\theta}}(60)$	12.2	8.8	7.3
V	11.6	13.3	13.9
$\sigma_{\widetilde{v}}(60)$	1.08	0.88	0.76
$\sigma_{\widetilde{v}}(10)$	0.75	0.53	0.50
R	1.24	2.21	1.86
N	17	10	27
	1300 – 1400 EST,Winter		
$\sigma_{\widetilde{\theta}}(60)$	14.7	11.0	7.2
V	6.8	9.4	6.3
$\sigma_{\widetilde{v}}(60)$	1.75	1.69	0.75
$\sigma_{\widetilde{v}}(10)$	1.30	1.16	0.50
R	0.90	1.37	1.77
N	12	21	11
	1300 – 1400 EST, Summer		
$\sigma_{\widetilde{\theta}}(60)$	19.3	9.7	7.8
V	7.1	8.8	7.2
$\sigma_{\widetilde{v}}(60)$	2.28	1.49	0.85
$\sigma_{\widetilde{v}}(10)$	1.67	0.99	0.46
R	0.95	1.76	2.72
N	13	23	11

Table 2 (continued).

	City	New Jersey	Bay

$1\frac{1}{2} - \frac{1}{2}$ Hours Before Sunset, Winter

	City	New Jersey	Bay
$\widetilde{\sigma_\theta}$ (60)	19.3	9.7	7.8
V	7.1	8.8	7.2
$\widetilde{\sigma}_v$ (60)	2.28	1.49	0.85
$\widetilde{\sigma}_v$ (10)	1.67	0.99	0.46
R	0.95	1.76	2.72
N	13	23	11

$1\frac{1}{2} - \frac{1}{2}$ Hours Before Sunset, Summer

	City	New Jersey	Bay
$\widetilde{\sigma_\theta}$ (60)	29.2	11.0	8.8
V	4.2	5.9	7.7
$\widetilde{\sigma}_v$ (60)	2.11	1.09	0.97
$\widetilde{\sigma}_v$(10)	1.32	0.63	0.51
R	1.70	2.10	3.00
N	17	19	11

2. RESEARCH AT NATIONAL REACTOR TESTING STATION, IDAHO

2.1 Some Mesoscale Transport Results From 1969 Data

In an attempt to establish a climatology of the transport of effluent from various release locations at the National Reactor Testing Station (NRTS) a method has been established, as described in an earlier report, for computing and displaying trajectories of hypothetical particles serially released and transported by the winds obtained from the mesoscale tower network (ESSA Tech. Memo. ERLTM-ARL 17, 1970). A sample case covering three days was selected and presented for illustrative purposes. Since then, trajectories for hypothetical particles, serially released with a separation of 1 hour, have been computed and plotted for the first 7 months of 1969. Presented here is a preliminary summary of the results and some of the 420 diagrams produced, showing characteristics that seem representative of several distinct classes of transport.

The geographical layout of the valley, locations of the wind stations, and the site boundaries are shown in figure 9. For scaling purposes, note that the northern boundary of the site is 10.67 mi long. Table 3 is reproduced here from the earlier report for assistance in determining the time of various particle positions from the symbols on the trajectory plots. It should be pointed out here that these diagrams were produced by computer, which often results in poor drafting by superimposing symbols and drawing lines through symbols. However, since the plots are used as a research tool, a compromise was made between practicality and esthetics.

Examination of the trajectory plots for the first 7 months of 1969, for particles released from a location in the southwestern portion of NRTS, reveals a variety of transport. Because climatological data, in the form of wind roses, indicates the prevailing wind directions over the area to be southwest and northeast, one would expect a good deal of the transport to be in these directions. The complicating factor, however, is that the wind direction is quite frequently subject to a diurnal reversal. In addition to this, there is evidence, in the earlier report cited above, that the boundary layer mesoscale winds are occasionally influenced dramatically by synoptic scale features. These transient conditions produce the variety of transport conditions, as demonstrated by the trajectories for a few representative days presented in figures 10 through 13.

We note in figure 10a that the wind is from the northeast from 0100 MST through 1400 MST March 7, 1969, at which time it shifts rather abruptly to the northwest. The trajectories in figure 10b show that in the next 12 hours the wind direction turns through another 270^{0} back to a northeasterly direction, resulting in a significant spreading of the stream of particles. Figures 10 c, d and e show that the wind direction affecting particles from this release point stays northeasterly with minor variations for the next 43 hours. There is a 4-hour excursion to an easterly direction in figure 10f before the wind direction shifts back to the northeast until about 11:00 MST March 4, when it shifts to a westerly direction carrying 9 of the 12 particles in figure 10g in a fairly narrow band off to the east. Note the contrast in the spread of the particles from that in figure 10b.
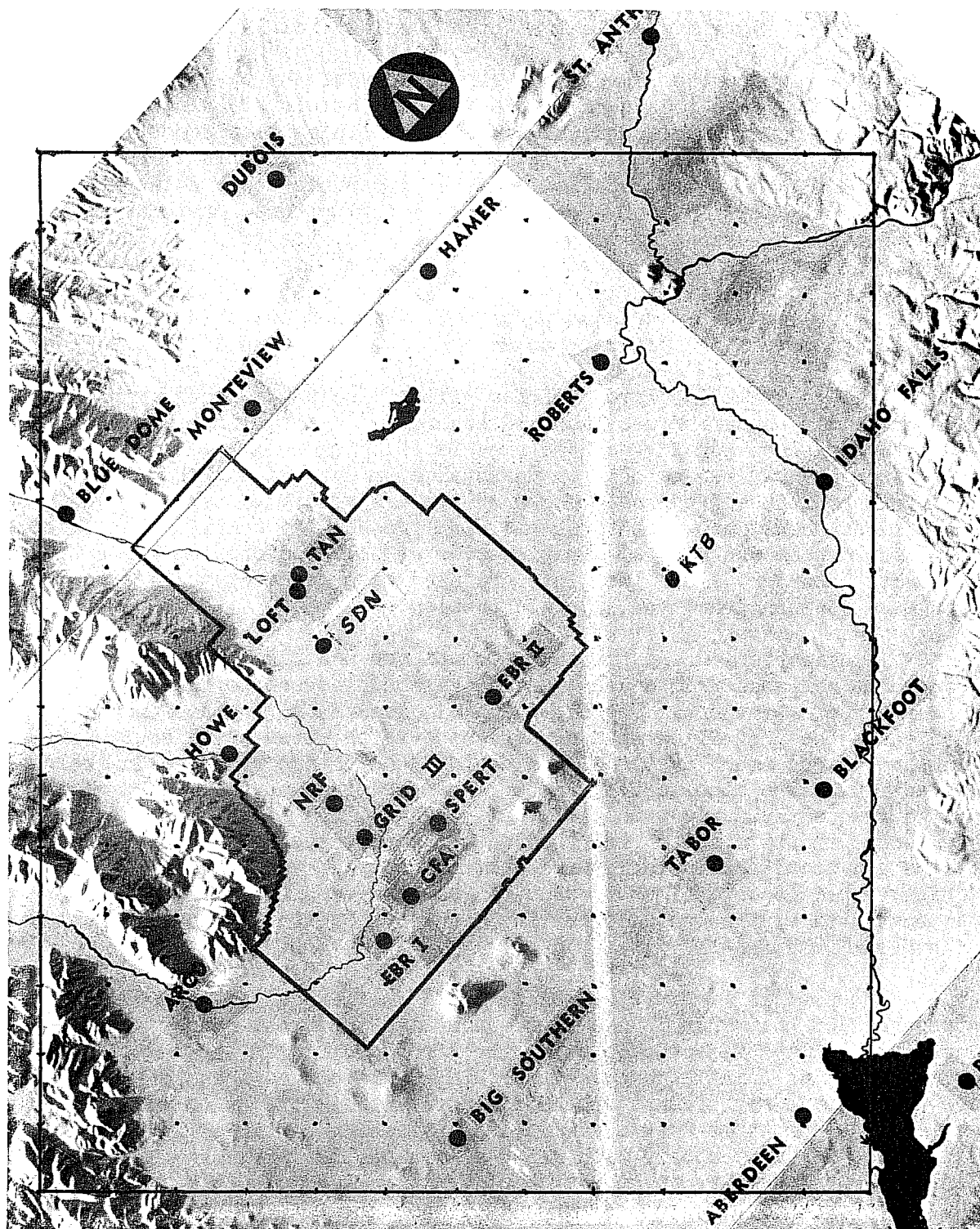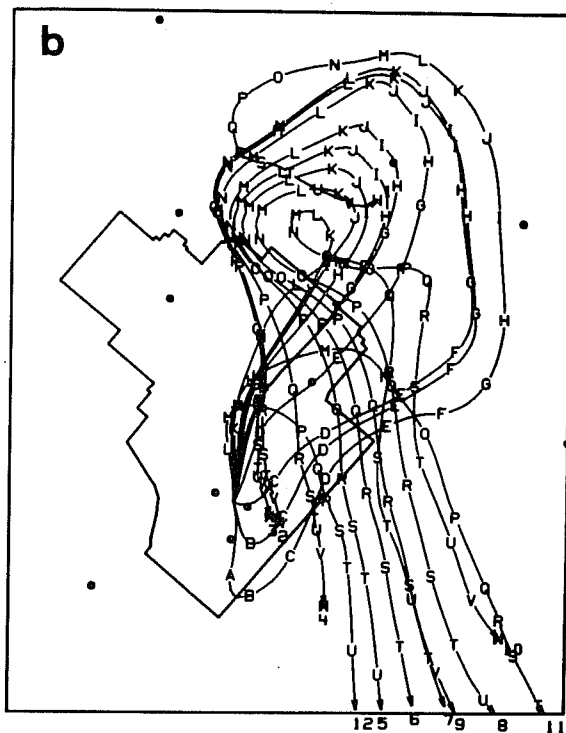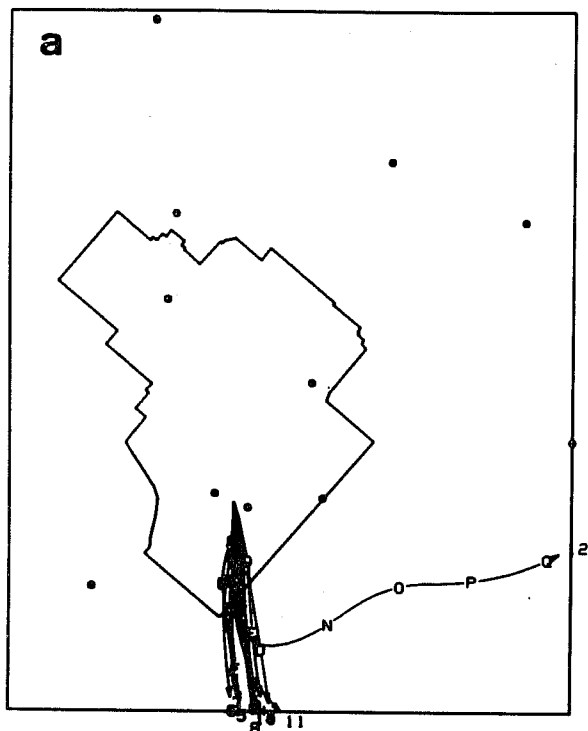
Figure 9. The geographical area covered by the computational
grid. The separation of the grid points is 5.33 mi.
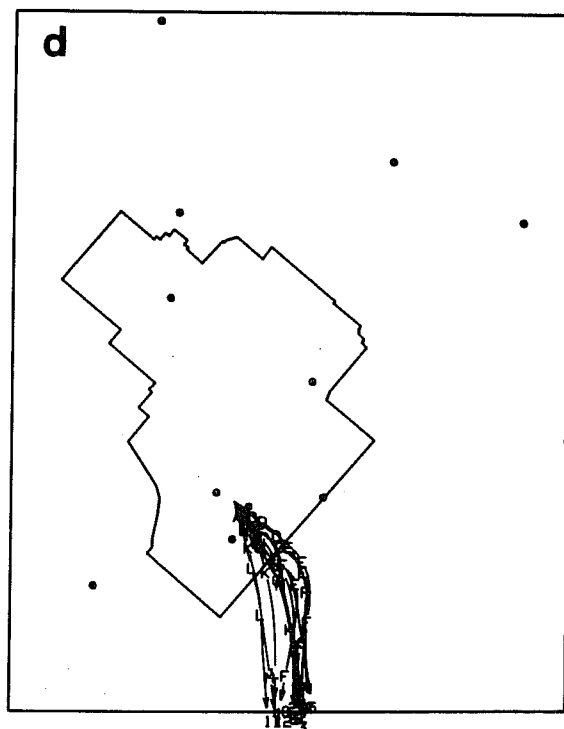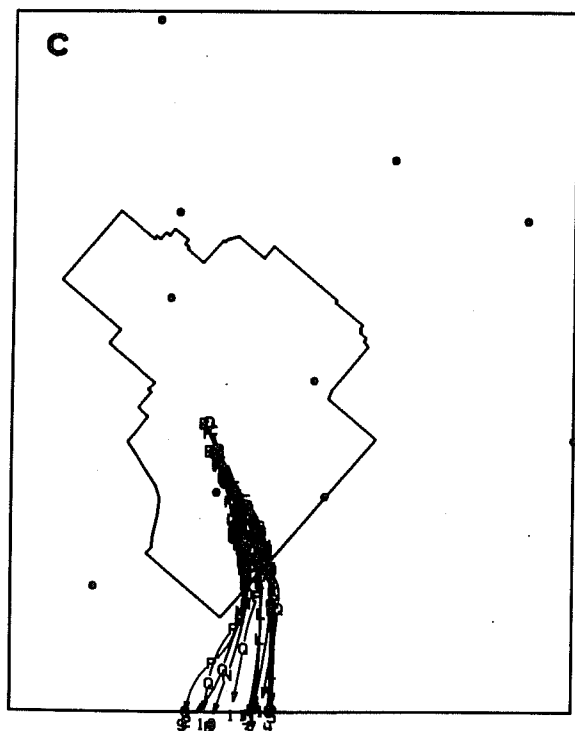
Table 3. Symbols for Particle Trajectories.[*]

Release Duration 0100 – 1200 MST			Release Duration 1300 – 2400 MST		
1		1:00	1		13:00
2	A	2:00	2	A	14:00
3	B	3:00	3	B	15:00
4	C	4:00	4	C	16:00
5	D	5:00	5	D	17:00
6	E	6:00	6	E	18:00
7	F	7:00	7	F	19:00
8	G	8:00	8	G	20:00
9	H	9:00	9	H	21:00
10	I	10:00	10	I	22:00
11	J	11:00	11	J	23:00
12	K	12:00	12	K	24:00
	L	13:00		L	1:00
	M	14:00		M	2:00
	N	15:00		N	3:00
	O	16:00		O	4:00
	P	17:00		P	5:00
	Q	18:00		Q	6:00
	R	19:00		R	7:00
	S	20:00		S	8:00
	T	21:00		T	9:00
	U	22:00		U	10:00
	V	23:00		V	11:00
	W	24:00		W	12:00

[*] The particle numbers appear opposite their release times. The hourly particle position is indicated by the appropriate letter – time combination.
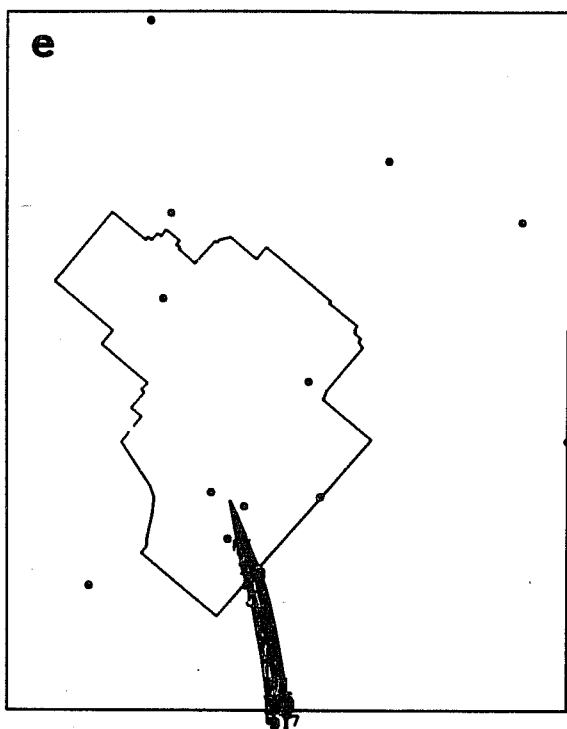
Figure 10.   Trajectories of hypothetical particles released hourly and transported by a time series of objectively interpolated wind fields.   Particle numbers appear at the ends of the trajectories.
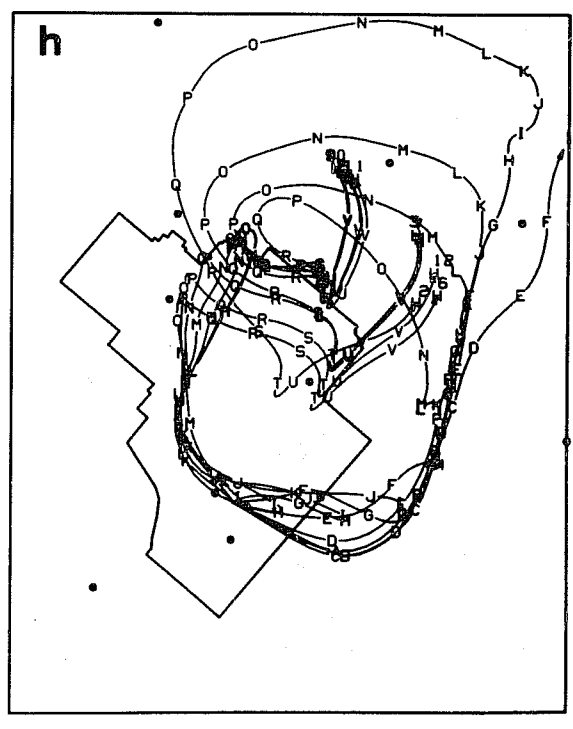
22

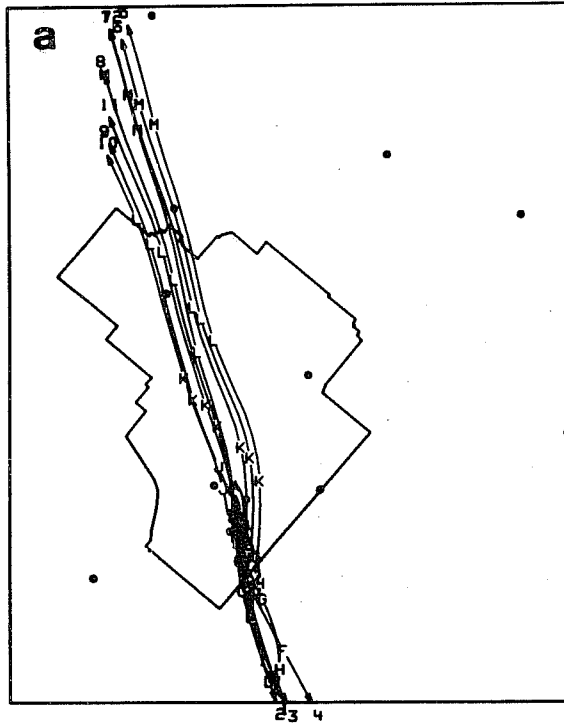Figure 10. Trajectories of hypothetical particles (continued).

23
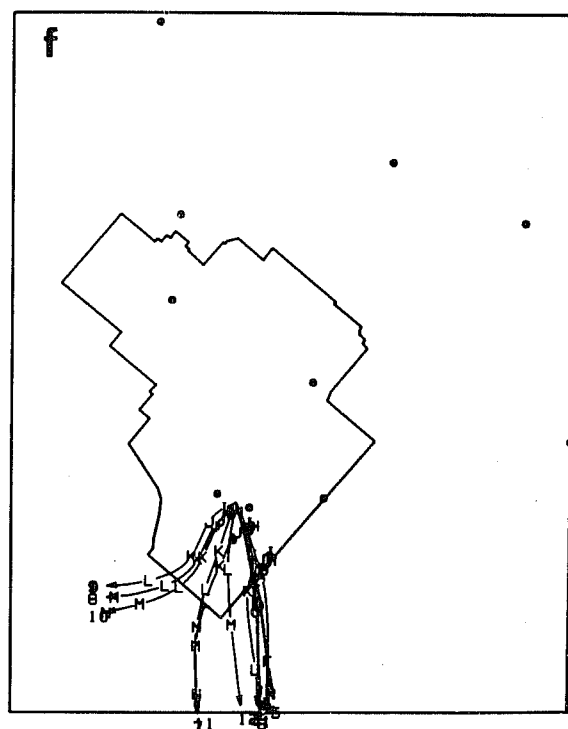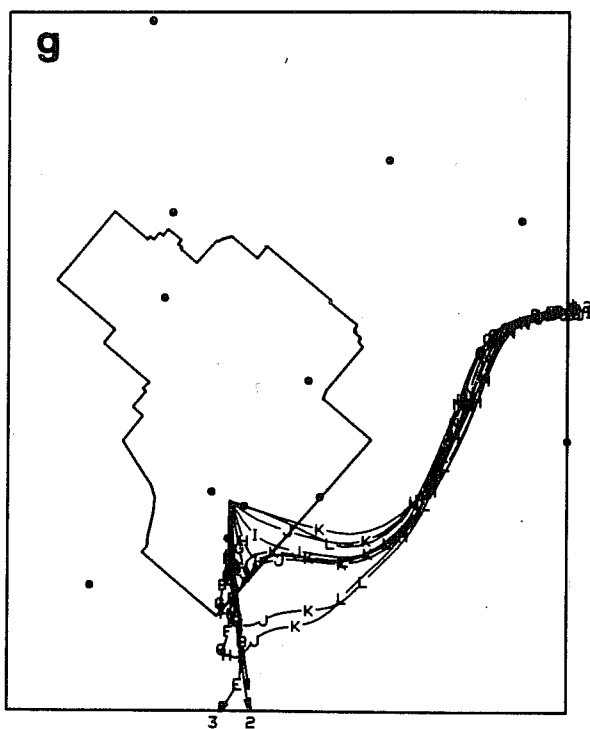
In figure 10h we have an example of the transitions in wind direction and variation in direction over the grid that cause all except particle 1 to remain on the grid for the 24-hour advection period. As the particles in the upper right quadrant of the grid begin to move in a northerly direction at positions K (2400 MST), the particles at the release point also begin moving toward the north. However, between 0300 and 0600 MST they move toward each other and meet in the northern portion of the site, and between 0600 and 0900 they move southward as a group. Between 0900 and 1000 MST they turn east, and by 1200 MST they have begun to turn northward again. This type of trajectory pattern seems to suggest the existence of a mesoscale eddy of the type shown in the earlier report cited above. The eddy phenomenon is demonstrated again in figure 11d, and the wind fields showing this eddy are presented in figures 12a and b.

Another phenomenon, suggested previously (Dickson, 1967), is the formation of a line source, from the effluent from a point source, by a sudden change in wind direction. This is shown quite clearly in figures 11a, e, and g. In these diagrams the direction reversals are fairly sudden, and the width of the area covered by the particles is fairly small. In figure 11g, particles 6 and 12 turn suddenly southeastward by 1600 MST and move across the valley at about 12 mph. It is very likely that the others would have followed had they not left the computational grid before the wind shift. This sudden shift is followed by a slower one shown by the spray of trajectories in figure 11h.

Figure 13 is an attempt to show the effect of the location of the release point through a series of diagrams that are coincident in time with the diagrams in figure 11, but the release point is 25 mi to the north-northeast. Note in figure 13d that the particles from the northern release point seem to get caught in the same eddy as those from the southern release point; also, as shown in figure 13e, stronger northerly winds at the northern release site carry the particles as far south, before the direction reversal, as those released from the southern release point. In figure 13f, particles 10, 11, and 12 are caught in a reversal between 2300 and 2400 and are carried south and then east across the entire valley, whereas the particles with the same numbers released at the southern release point (see fig. 11f) are carried north and then after the reversal to the south end of the site where they loop in a westerly direction. The first two trajectories in figure 13g follow the same pattern as those in figure 13f. Particle 3, however, moves northward from 2300 MST July 5 until about 0400 MST July 6, when it is caught in a reversal and moves southward off the computational grid. Had particles 1 and 2 not left the computational grid they would probably have shown the same reversal. This is another indication that our observational network is too small to adequately handle the problem of recirculation.

Although qualitative, the results presented and discussed here provide information about some distinct characteristics of low-level mesoscale flow patterns in the upper Snake River Plain. Results such as these indicate that effluent transport on this scale can be significantly more complex than the meandering plume in microscale transport. Examples of this are the formation of a line source from a point source, the wide variation in trajectory dispersion
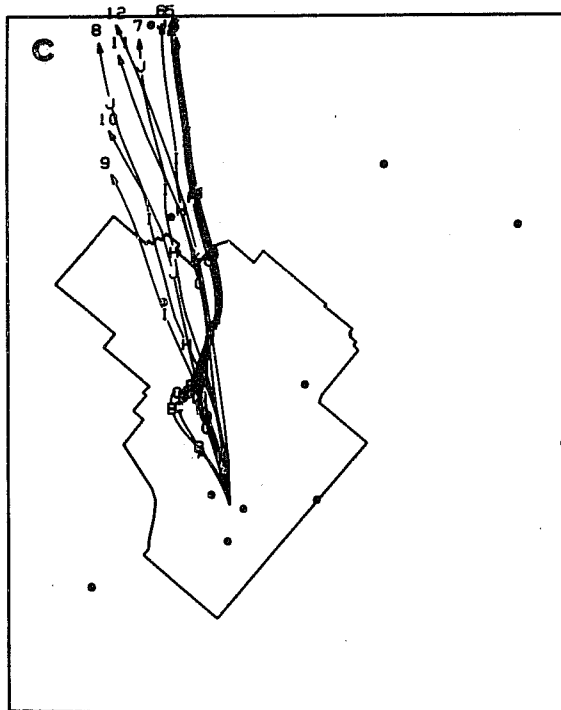
24

CPP RLSE 0100 07/02/69 TO 1200 07/02/69

CPP RLSE 1300 07/02/69 TO 2400 07/02/69
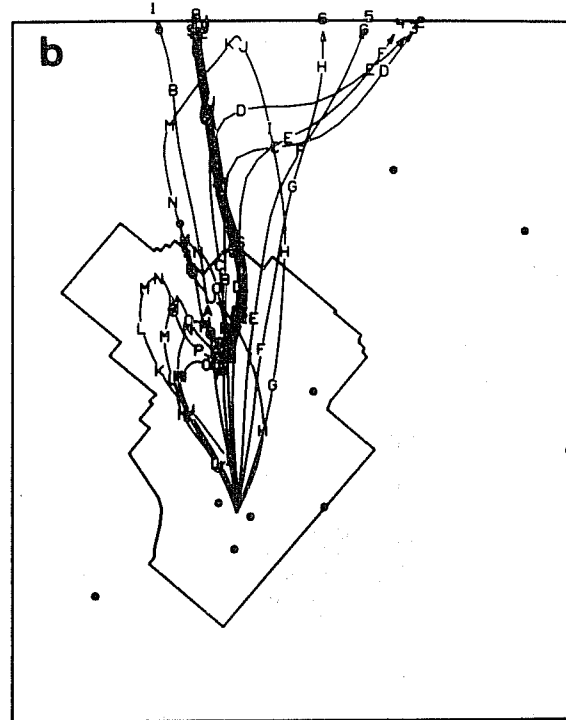
CPP RLSE 0100 07/03/69 TO 1200 07/03/69

CPP RLSE 1300 07/03/69 TO 2400 07/03/69

Figure 11. Trajectories of hypothetical particles. See fig. 9 for details.

25

Figure 11. Trajectories of hypothetical particles (continued).

26

Figure 12. Mesoscale flow patterns depicted by wind vectors obtained by spatial interpolation of hourly averaged winds.
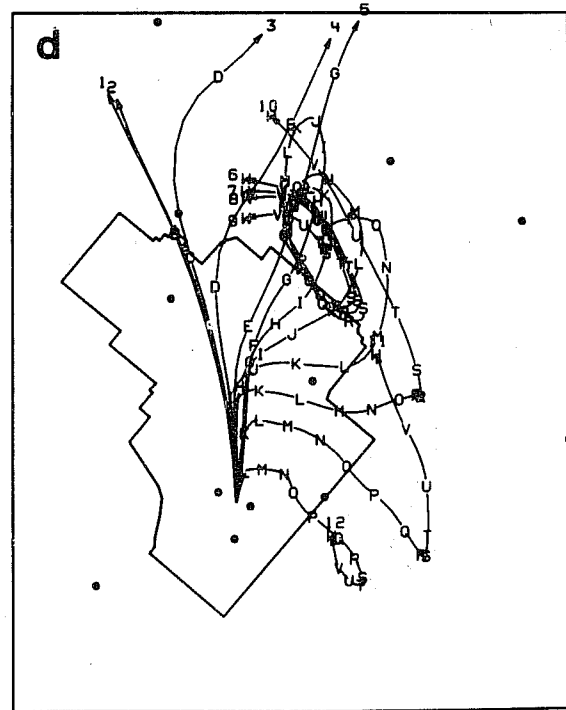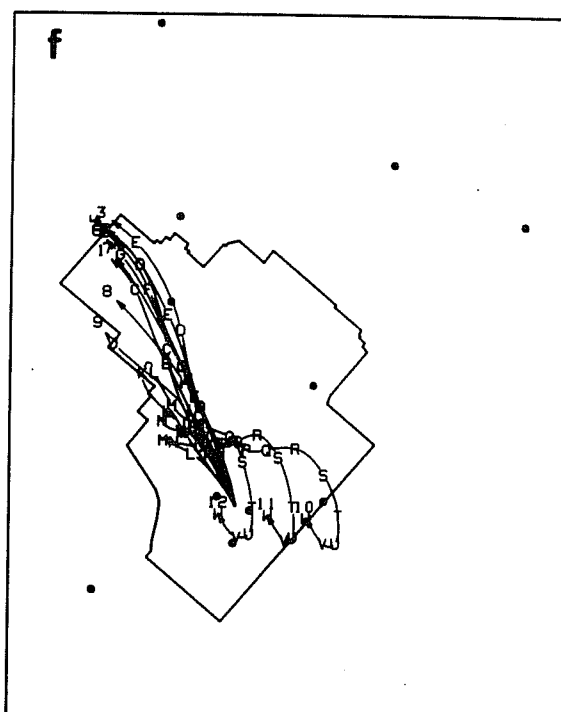
27

a

b

c

d

Figure 13.   Trajectories of hypothetical particles. See fig. 9 for details.

28
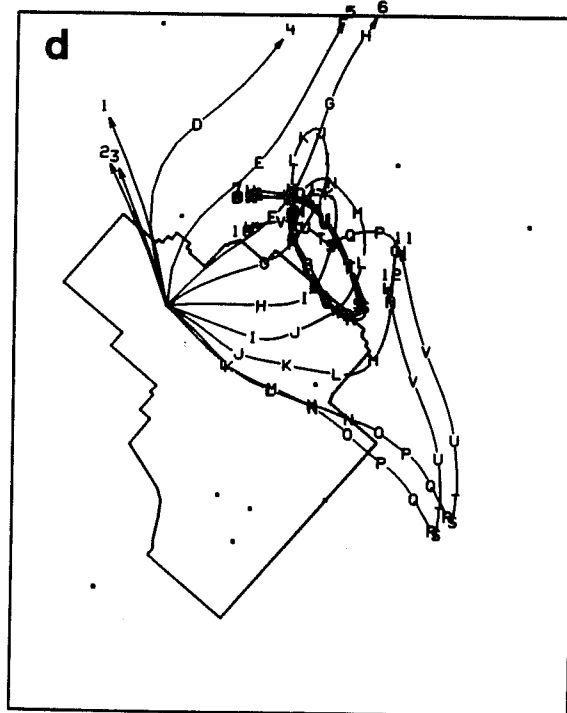
LOFT; 0100 07/04/69 TO 1200 07/04/69   LOFT; 1300 07/04/69 TO 2400 07/04/69
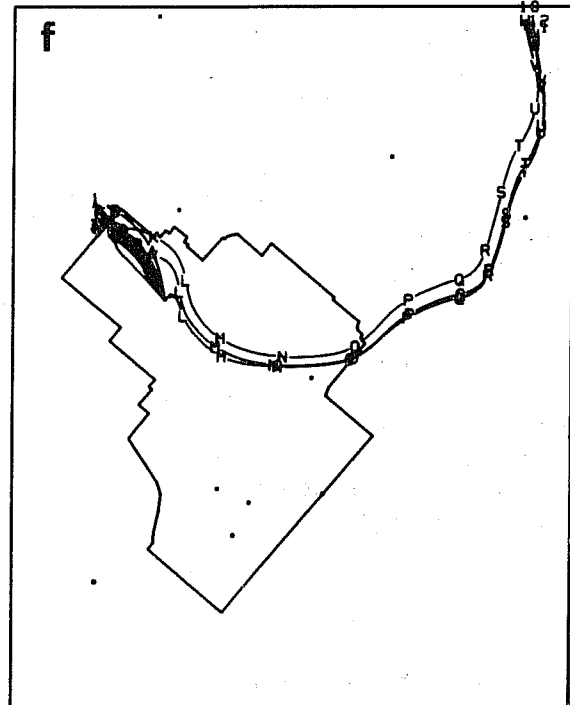
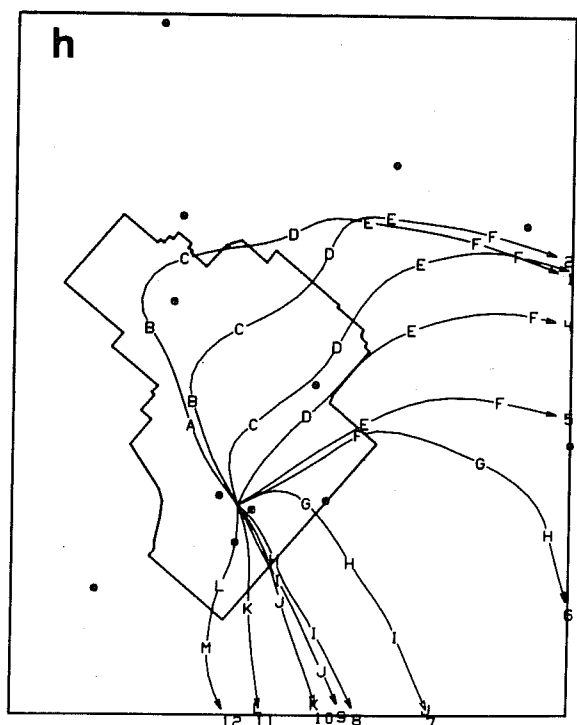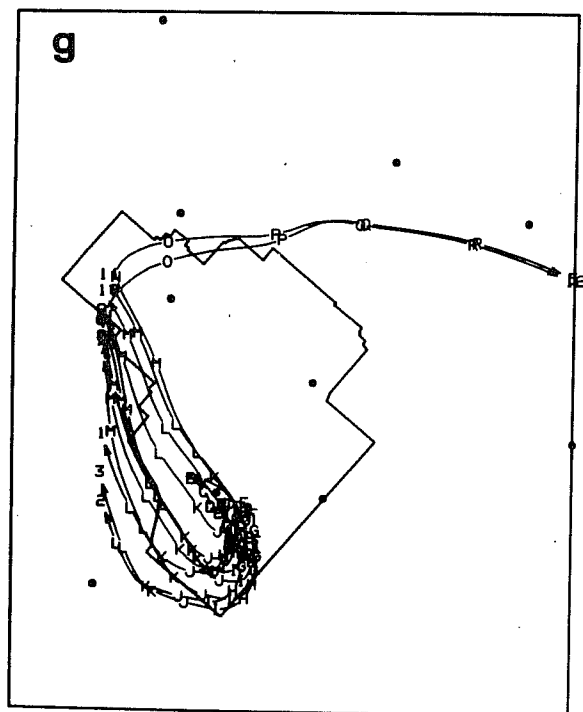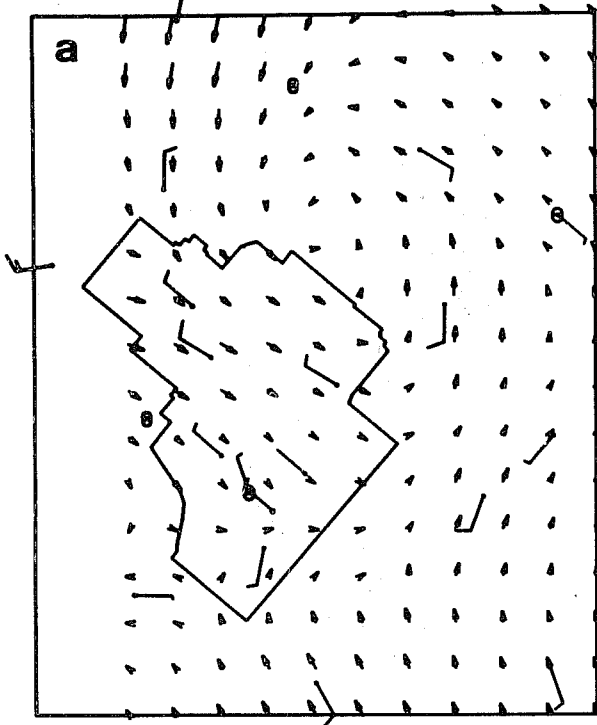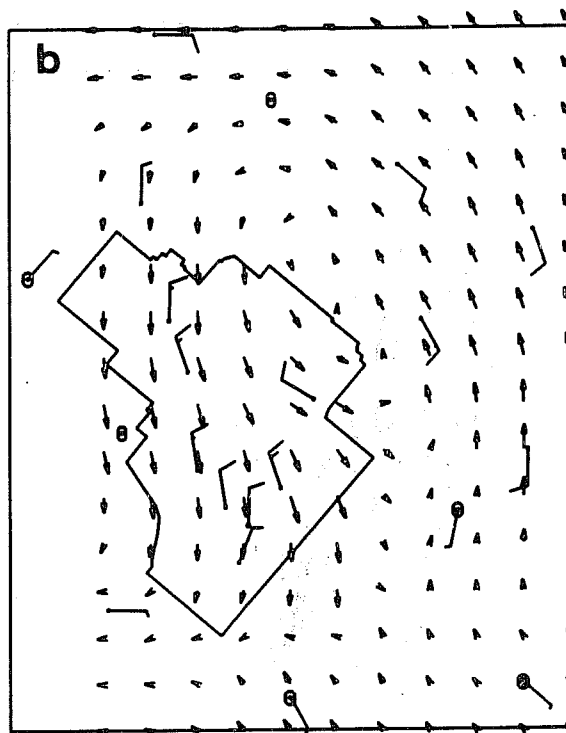LOFT; 0100 07/05/69 TO 1200 07/05/69   LOFT; 1300 07/05/69 TO 2400 07/05/69

Figure 13. Trajectories of hypothetical particles (continued).

29
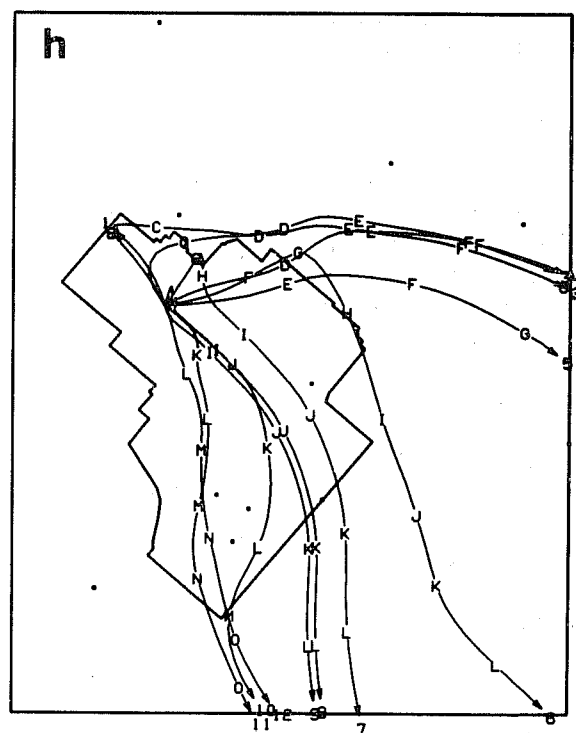
and the problem of recirculation. This means that the transport prediction problem is more difficult than originally anticipated. Work is proceeding to establish a more quantitative basis for a transport climatology.

The strong indication of a well-defined eddy 20 to 30 mi in diameter is also a facet that warrants further investigation. It suggests that there might be an area around the eastern boundary of the site with a higher than normal stagnation of particles.

As a reminder, these trajectories are not isobaric or isentropic, but merely an estimate of the approximate paths of particles that remain in a layer from 50 to 500 ft above the ground. The amount of error in the data and in the various processes required to obtain the trajectories is still under investigation. However, all things considered, they probably represent enough of an improvement over trajectories that would be obtained by a single station analysis to be worthy of consideration.

2.2 Accuracy Testing of Random-to-Grid Interpolation of Mesoscale Winds

To test a random-to-grid interpolation scheme, a method has been established for checking an interpolation value against some known value. A group of stations is selected for use in interpolating the quantity in question to some point at which the quantity is known. The method is applied to the wind data from the meso-network for three separate configurations of three stations each. For comparison, the data for each of the three separate sets of stations is interpolated to a fourth station, unique to each set, at which the wind direction and velocity have been measured. Statistics on the differences are then computed.

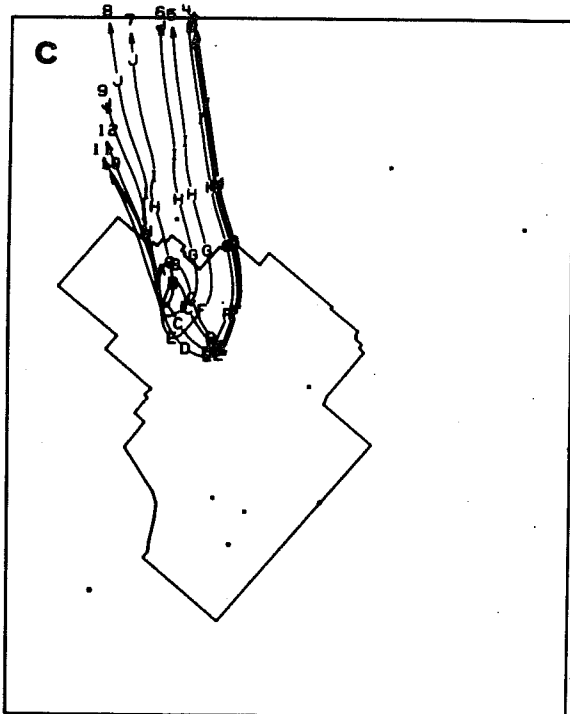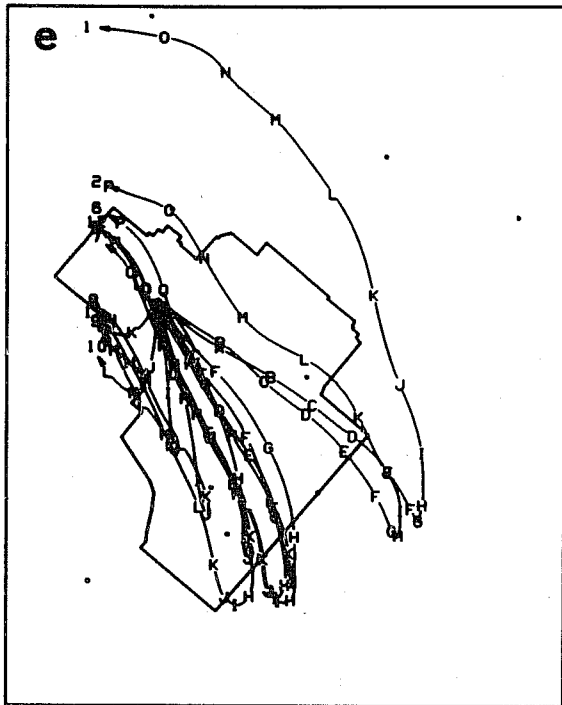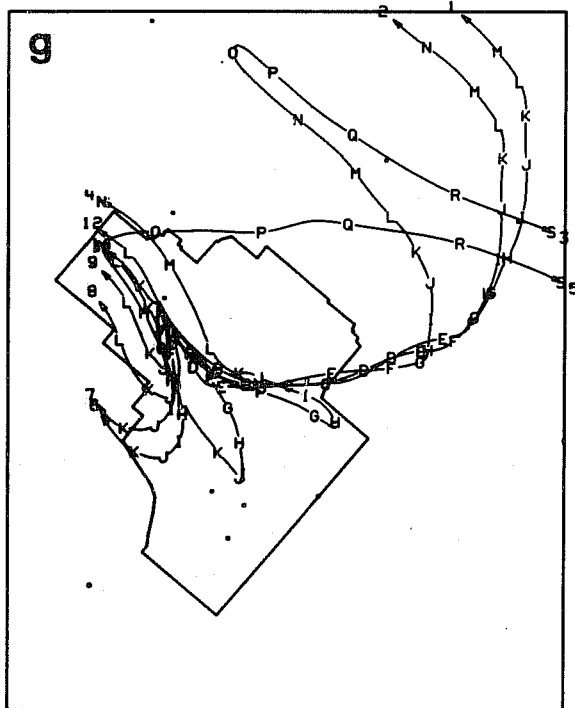The interpolation method tested here is the weighted averaging technique, in which the weighting factors are the inverse squares of the distances from the test station to the data stations. The wind data used consist of hourly averaged wind speeds and directions obtained subjectively from traces on strip charts. These directions and speeds are converted to wind components along and across the grid. The interpolated wind components obtained at the selected test station are converted to speed and direction for comparison with the speed and direction observed at the test station. The test stations and the stations used in the interpolations for each of the three configurations are shown in table 4. The spatial positioning of the stations is shown in figure 9. section 2.1. The monthly means and standard deviations of the direction (deg)/speed (mph) discrepancies are given in table 5. The discrepancies are obtained by subtracting the interpolated values from the observed ones. The word "discrepancy" instead of "error" is used here because of the possibility of error in the observed values.

30

Table 4. Stations Used in Interpolation Test.

	Case 1		Case 2		Case 3	
	Station I.D. and Sensor Height (ft)	Miles from CFA	Station I.D. and Sensor Height (ft)	Miles from SPRT	Station I.D. and Sensor Height (ft)	Miles from TAN
Test Station	CFA (250)		SPRT (50)		TAN (150)	
Stations used to interpolate	EBR I (50)	4.1	EBR 2 (240)	11.4	MTV (98)	13.3
	GRD 3 (200)	4.5	NRF (50)	7.4	NRF (50)	18.4
	SPRT (50)	3.9	EBR 1 (50)	8.3	EBR 2 (240)	18.1

Table 5. Monthly Means and Standard Deviations of Speed and Direction Discrepancies.

Month	Quant./Class	Case 1 ≥5 mph Stable	Case 1 ≥5 mph Unstable	Case 2 ≥5 mph Stable	Case 2 ≥5 mph Unstable	Case 3 ≥5 mph Stable	Case 3 ≥5 mph Unstable
Feb.	N	340	79	233	67	255	72
	Mean	-9/-4	-16/-2	15/-1	14/-2	24/-1	8/-2
	Std. Dev.	26/3	18/3	29/3	20/3	42/5	69/4
Mar.	N	220	50	178	47	200	34
	Mean	-9/-4	-11/0	15/-3	19/-3	20/-7	-14/-3
	Std. Dev.	21/2	12/1	28/3	29/3	62/8	61/6
Apr.	N	122	110	101	109	173	110
	Mean	-13/-4	-12/-1	31/-1	26/-1	25/-7	22/-5
	Std. Dev.	14/3	14/2	21/3	26/3	52/8	42/8
May	N	103	114	96	132	245	167
	Mean	-13/-5	-10/-1	-8/-2	-4/-2	-8/-4	-21/-4
	Std. Dev.	15/3	20/2	32/3	28/3	63/6	37/5
June	N	163	303	152	324	293	221
	Mean	-13/-5	-10/-2	-7/-2	-6/-2	-20/-5	-25/-3
	Std. Dev.	20/3	21/3	24/2	35/3	59/6	57/5
July	N	253	328	184	272	238	224
	Mean	-15/-5	-13/-2	-7/-2	-7/-3	-20/-5	-30/-6
	Std. Dev.	22/3	19/2	43/3	26/2	50/5	42/6

32

The criterion for considering an observation for an interpolated check was that the test station and all the reporting stations had to be showing wind velocities of 5 mph or greater. The stability determination for each observation was made from vertical temperature differences reported on the IET, EBR II, and CFA towers (see fig. 9 for location). The quantity N in table 5 refers to the number of observations in the given category that were available for the check. Each month has about 730 hours in which the check is possible if the wind criterion is satisfied and none of the stations are reporting missing data. The month of January 1969 was omitted from the table of results because of sensor problems at EBR I.

If we consider the results for case 1, in which the stations used for interpolation lie within a 5-mi radius of the test station, one of the first items to come to our attention is that in both the stable and unstable categories the monthly mean direction error is always negative. This means, according to the definition of the difference, that if one faces in the direction of the observed wind, the interpolated wind would be to the left. A bias as consistent as this would suggest a direction orientation problem involving one or more of the stations. Examining the mean discrepancies in wind speed shows that the interpolated wind is too slow by 4 to 5 mph for the stable case, but only by 1 to 2 mph for the unstable. This seems to be attributable to the fact that the test station observation is made at 250 ft, while observations for the stations used in the interpolation are from 50, 200, and 50 ft. Under stable conditions the vertical wind profile approaches the classical logarithm form and velocity differences in the vertical are greater than for the unstable case. When the speeds were all adjusted logarithmically to 100 ft, the same calculations show the mean speed discrepancies dropping to less than 1 mph, but there is no significant improvement in the standard deviation of the speed or direction discrepancies.

In considering the standard deviations of the discrepancies one has to keep in mind that the wind direction observations consist of a subjective average of a 4-to 5-inch long pen trace estimated to the nearest 10°. This, in itself, might be expected to contribute 5 to 10° to the standard deviation under the most favorable conditions. This means that the direction difference standard deviation for case 1, which varies from 12° to 26°, is quite reasonable. Since the speed observations are obtained in the same manner as the direction observations, the 1-to 3-mph standard deviations for the speed differences are also quite reasonable.

The results for case 2 (stations within a 12-mi radius) show a drastic change in the mean discrepancy for direction difference between the months of April and May. An orientation change was reported for the wind vane at EBR II May 9, 1970, which would explain the change from one month to the next. Since this same station was used in case 3, the same change occurred in the results. The standard deviations for direction discrepancy increase by about 10 to 15° from case 1 and the velocity standard deviations increase by about 1 mph.

For case 3 (stations within a 20-mi radius) the standard deviations show an inordinate jump of 20 to 30° for direction difference and 4 to 5 mph for speed difference. Closer examination of the topography indicate that the large standard deviation of the discrepancies are probably attributable to the fact that the test station, TAN, lies just beyond the mouth of a canyon, which would have little or no effect on the stations used for interpolation. This should be no reflection on the operational interpolation to grid points in this vicinity, however, because stations TAN and SDN would be used in the process. For testing the interpolation scheme for a large radius of influence, other station configurations have been selected.

The primary disadvantage of this type of test of the interpolation scheme is that the discrepancies include both the effects of interpolation and error in the original data. Comparisons of observed and interpolated wind direction and speed, hour by hour, indicate that the discrepancies are not Gaussian. Because occasional large discrepancies that would significantly affect the standard deviation were traced to an error in the original data, an objective scheme has been developed in an attempt to detect this error, in order to correct the data or discard them for use in computations.

2.3 Kinematic Modeling of Mesoscale Flow

In determining the characteristics of mesoscale flow patterns by objectively interpolating to a regularly spaced grid from a finite number of randomly spaced wind stations, one has to consider whether this method is a realistic one. Two main factors seem to be involved: the spacing of the stations and the accuracy of the data from each station. Since, when one deals with real data, these two factors are not distinguishable, it is advantageous to test the interpolation scheme on mathematically modeled flow.

The modeling technique used here is similar to the one used by Saltzman (1959) for a different purpose. The flow over the field of interest is defined by a stream function found in Fourier fashion as a collection of a number of harmonic components:

$$\psi(x,y,t) = \sum_{i=1}^{N} A_i \cos m_i\{x - U_i(t + TX_i)\} \cos n_i\{y - V_i(t - TY_i)\} \qquad (1)$$

where A_i represents the amplitude of each harmonic, m_i and n_i are the wave numbers in the x and y direction respectively, U_i and V_i are the x and y components of the speed of motion of each harmonic, and TX_i and TY_i are the initial time displacements of each component in the x and y directions respectively. The wave numbers in the x and y directions are obtained by dividing the x and y lengths of the computational grid by the x and y wave-lengths of each harmonic. For greater flexibility in specifying the size and shape of each harmonic, they are not required to be integers in the analysis presented here.

34

Since we are interested in observing the characteristics of the wind patterns, we use the relationships

$$u = -\frac{\partial \psi}{\partial y}$$

$$v = \frac{\partial \psi}{\partial x} \tag{2}$$

to obtain the x and y components of velocity at any point on the grid at any particular time. The results are

$$u(x,y,t) = \sum_{i=1}^{N} A_i n_i \cos m_i \{x-U_i(t+TX_i)\} \sin n_i \{y-V_i(t-TY_i)\} \quad ,$$

$$v(x,y,t) = -\sum_{i=1}^{N} A_i m_i \sin m_i \{x-U_i(t+TX_i)\} \cos n_i \{y-V_i(t-TY_i)\} \quad . \tag{3}$$

To test the computational scheme and analyze each component separately, values of u_i and v_i are computed for each grid point and each station location and are displayed in the same manner as the mesoscale analyses of real data. Examples of this for N = 3 components are shown in figures 14D and 15D. Values of the controlling parameters are shown in table 6. Component 1, shown in figure 14A, consists of a pattern of alternating cyclonic and anticyclonic elliptical eddies moving in the y direction at 2.5 mph. Each eddy is twice as long and twice as wide as the computational grid. This combination of size and motion results in a complete wind direction reversal every 12 hours. The second component of the hypothetical motion, shown in figure 14B, is a collection of alternating cyclonic and anticyclonic eddies moving at 2.83 mph at a 45° angle to the computational grid. Each eddy is 21-1/3 mi in diameter. Component 3, shown in figure 14C, is specified to be a light wind (about 5 mph) in the y direction. The results of combining these three components of motion is shown in figure 14D. The same modeled flow is shown 3 hours later in figure 15. Both the winds at the regular grid points shown as vectors and the winds depicted by the standard wind symbols were obtained from the model in (3).

To obtain the winds at the grid points by whatever objective method we may choose, we can now use the winds at the station as if they were actual winds. Comparison of the winds obtained objectively with the modeled winds at the grid points will demonstrate the validity of the method for the station spacing used. An example of this type of comparison is shown in figures 16A through 16H. The modeled winds at both the wind stations and the grid points are shown on the left. The same modeled winds at the stations and the interpolated winds at the grid points are shown on the right. The interpolation method used here is the weighted averaging technique described in ESSA Tech. Memo. ERLTM-ARL 17 (1970).

(A) 300 MST DAY 1   COMP. 1

(B) 300 MST DAY 1   COMP. 2

(C) 300 MST DAY 1   COMP. 3
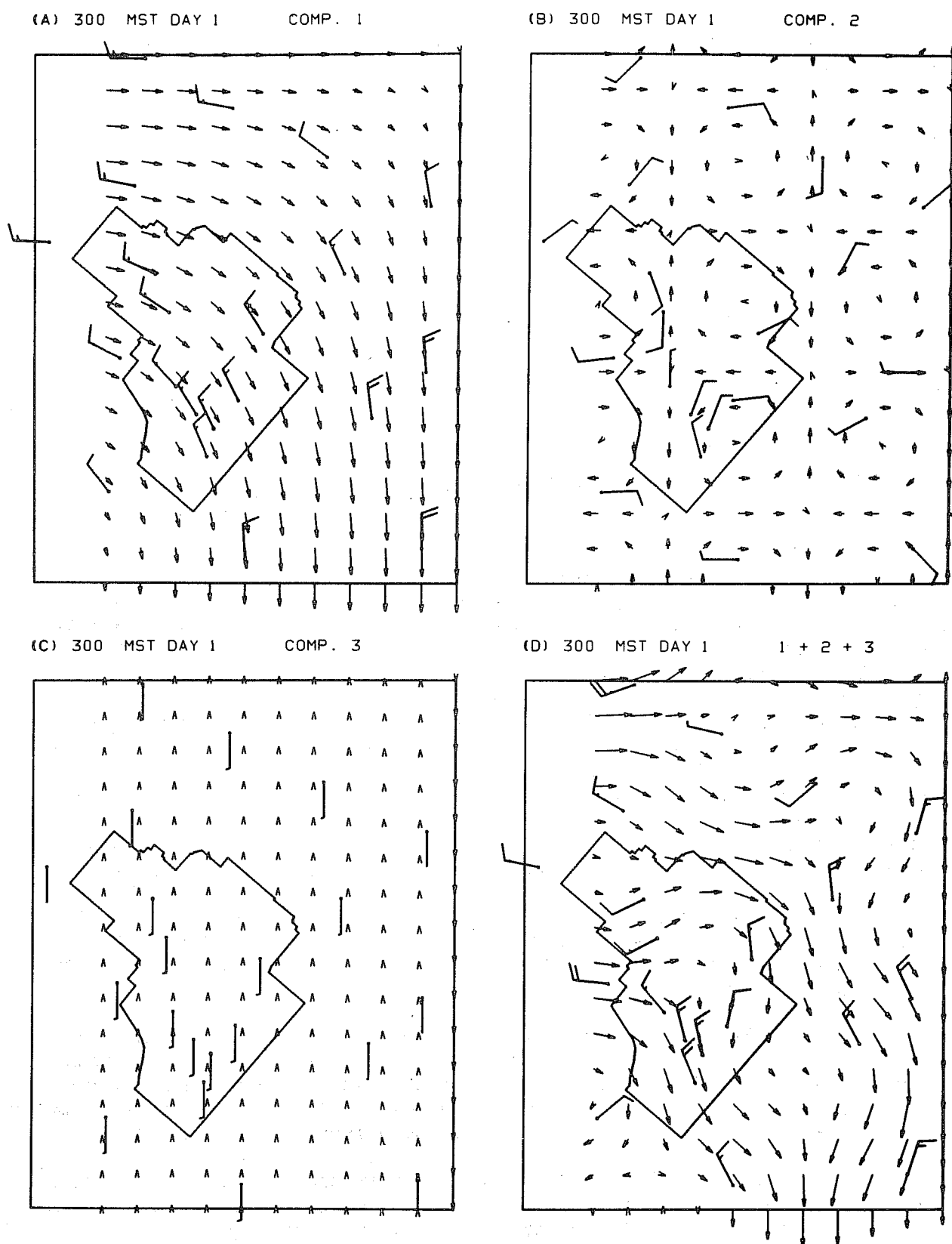
(D) 300 MST DAY 1   1 + 2 + 3

Figure 14.   Modeled mesoscale flow. The harmonic components are shown in (A)-
(C) and the combincation of all three components is shown in (D).

(A) 600 MST DAY 1   COMP. 1

(B) 600 MST DAY 1   COMP. 2

(C) 600 MST DAY 1   COMP. 3
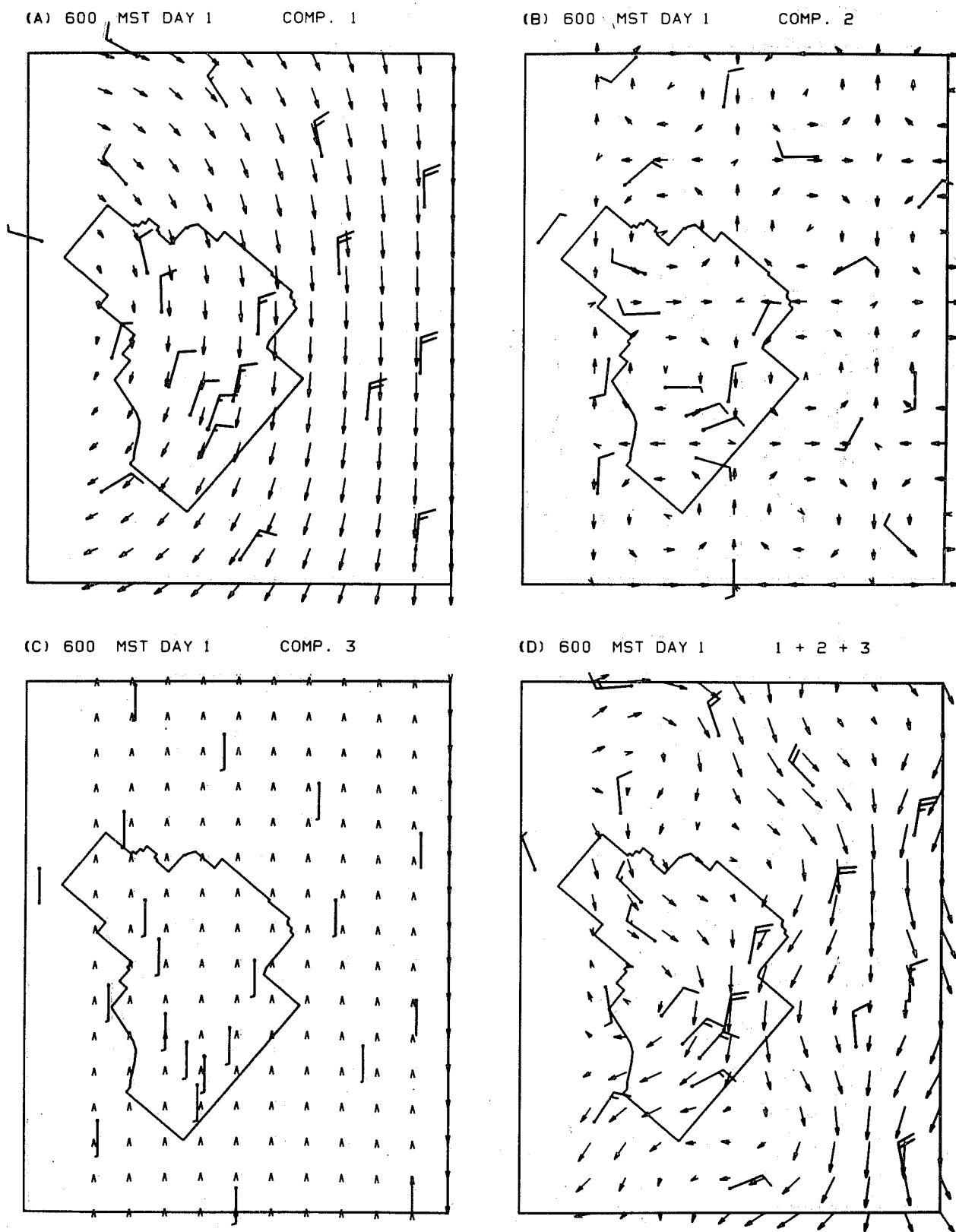
(D) 600 MST DAY 1   1 + 2 + 3

Figure 15.   Modeled mesoscale flow.   See fig. 9 for details.

(A) 300 MST DAY 1 MODELED
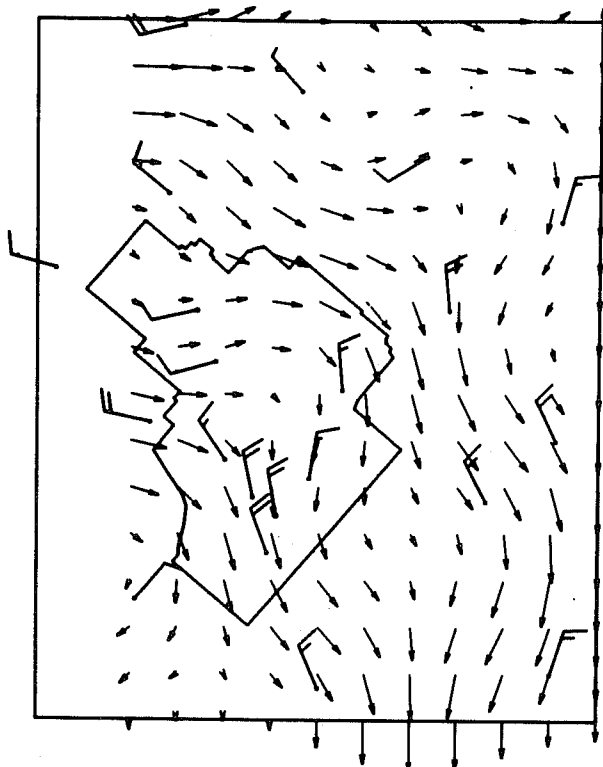
(B) 300 MST DAY 1 INTERPOLATED
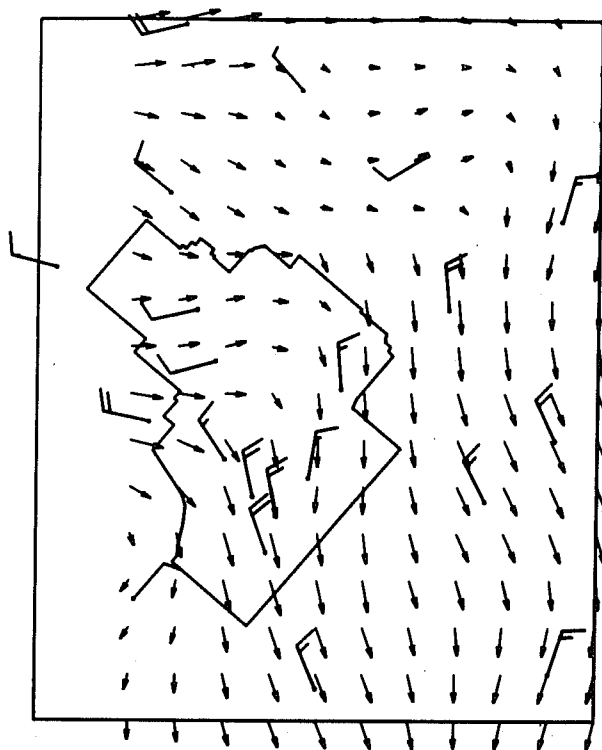
(C) 600 MST DAY 1 MODELED
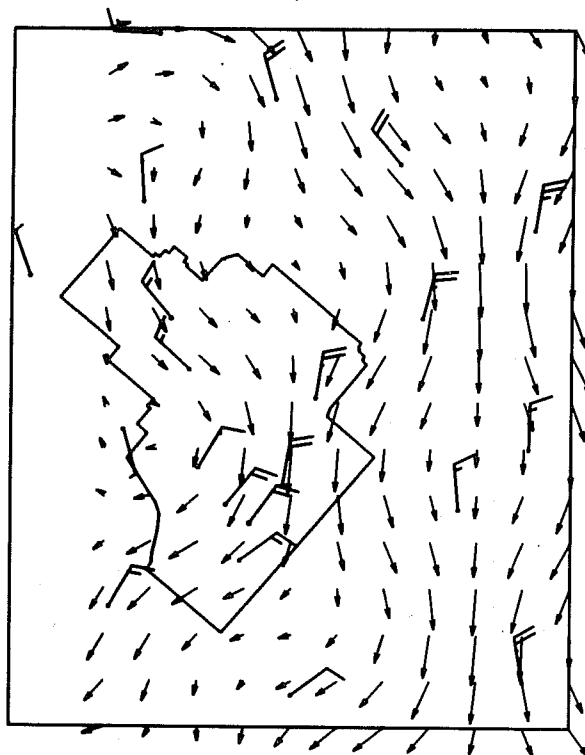
(D) 600 MST DAY 1 INTERPOLATED
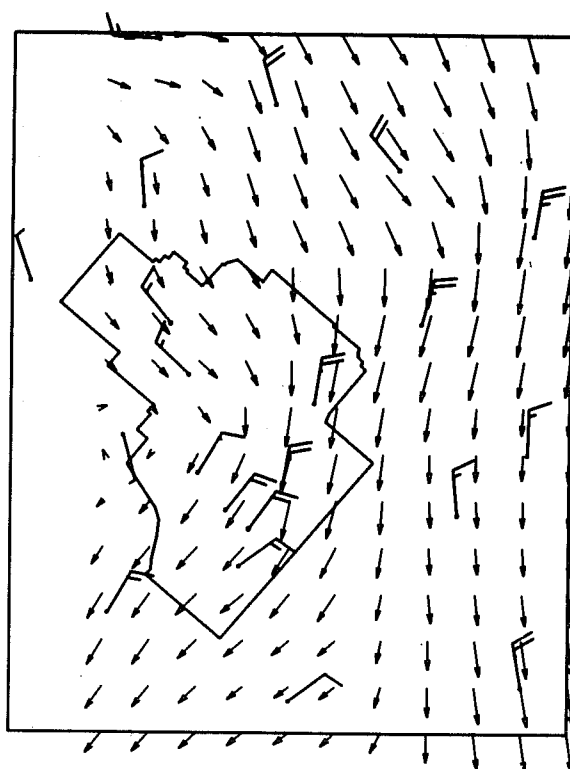
Figure 16. Comparison of modeled and interpolated flow.

(E) 900 MST DAY 1   MODELED
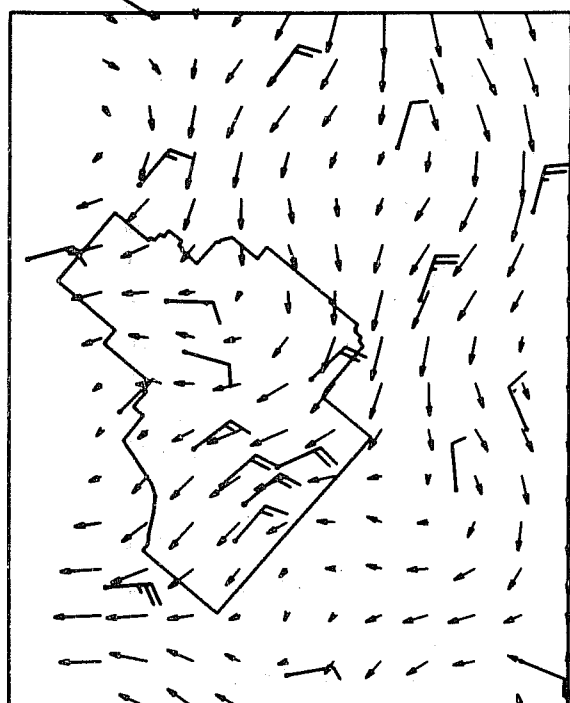
(F) 900 MST DAY 1   INTERPOLATED
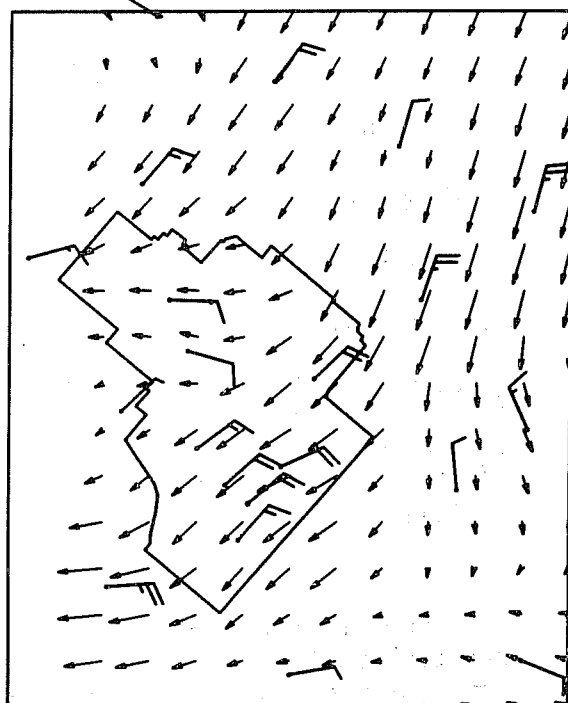
(G) 1200 MST DAY 1   MODELED
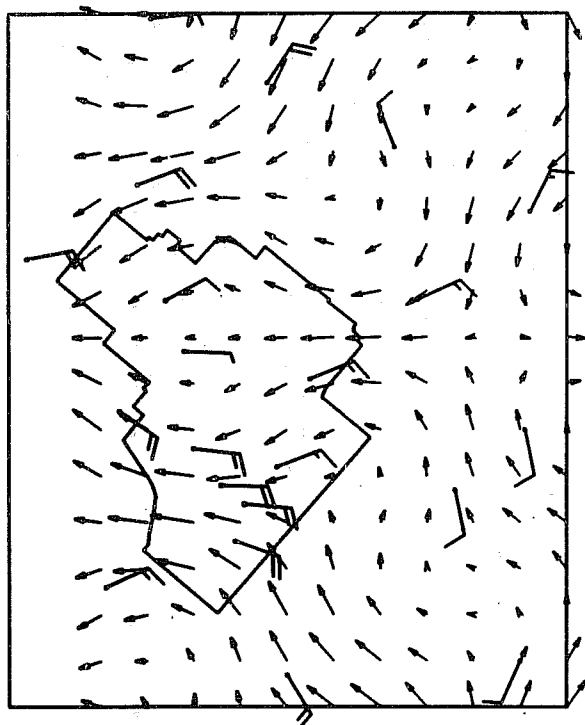
(H) 1200 MST DAY 1   INTERPOLATED
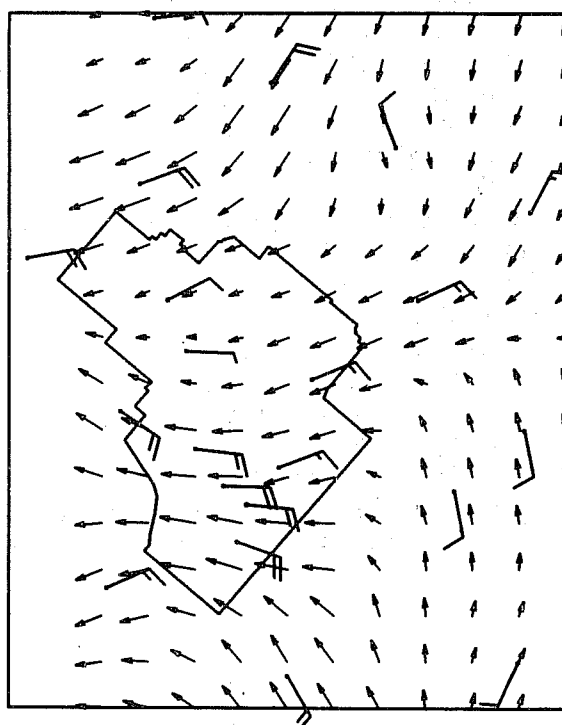
Figure 16.   Comparison of modeled and interpolated flow (continued).

Table 6. Modeled Flow Parameters.

	Comp. 1	Comp. 2	Comp. 3
A_i miles hour^{-1}	152.79	12.73	10.00
m_i no units	0.25	1.50	0.50
n_i no units	0.25	1.88	0.0
U_i miles hour^{-1}	0.0	2.0	0.10
V_i miles hour^{-1}	2.50	2.0	0.0
TX_i hours	0.0	0.0	110.0
TY_i hours	-3.0	-3.0	0.0

Since this work was still in the developmental stage at the end of this reporting period, only qualitative comparisons are made here. For the most part, the modeled winds at the grid points seem to be reproduced reasonably well, except in the upper right corner of the grid and two other areas within the grid. The latter two areas contain no wind stations and are centered halfway between Roberts and SDN and between Tabor and EBR-I (see fig. 9), respectively, and are both about 32 mi in diameter. Since the eddy size of component 2 in the model was about 21 mi, any objective interpolation method would be difficult to apply in these areas. This suggests that in order to give the interior part of the grid a chance of detecting eddies down to a minimum size of 20 mi new stations are needed in the vicinity of the center points given for these areas. With the existing grid setup, this is the smallest size eddy we can be concerned with. It might be argued that the requirement for these two station locations could have been determined without any data at all. However, the main purpose of this modeling technique is to test the effect of interpolation schemes on the transport of material by the wind field and we therefore must deal with some sort of data. It is hoped that by sensitivity analyses of trajectories from modeled wind fields, the effects of interpolation methods and errors in the data can be determined separately. Also, the flexibility in specifying the components of the modeled flow and the opportunity for comparison with real data may yield some knowledge about the makeup of mesoscale flow. An investigation of smaller eddy sizes (Baynton, 1967) showed no evidence of a coherent eddy structure from .5 to 6 mi in 112-hour samples of data obtained over a 12-day period.

2.4 Efficient Map Types

Earlier map typing experiments in which the Lund method of linear correlations between pairs of maps was used resulted in 15 to 30 map types, a cumbersome number for ready identification in real field forecast operation. The results of a modified Lund method is presented here.

Two conflicting arguments influence the level of significant correlation used in the Lund map typing method. The higher the level of significance, the greater is the similarity of maps classified into a type, and hence the climatology of weather events associated with each type is more meaningful. The converse argument is that the higher the level of significance, the greater is the similarity between types, the fewer are the cases within the types, and the greater is the number of cases not included in any type.

If the typing is done with the addition of a second significant correlation, the advantages of the higher level of significance in the basic Lund method can be retained and the disadvantages eliminated to a large extent. The first significant correlation is the level above which any pair of maps is considered significantly correlated. The second significant correlation is the level above which no two types can be correlated.

Map types for December–February of 1961–62 through 1967–68 were derived by the basic Lund method and the "two–correlations" method. The data were the 700–mb D–values at 1200 GMT taken from the NMC grid points in figure 17. There were 35 missing maps, resulting in a sample size of 595. The level of significance used in the experiment with the basic Lund method was 0.80, and the two correlations used in the second experiment were 0.85 and 0.70 respectively.

For both experiments the climatology of cases with each type is taken to be all maps from the original sample which are significantly correlated to each type map. This allows any map that is not a type map to be included in the climatology of more than one type so long as it is significantly correlated to each of the several types.

Table 7 shows the number of cases of each derived map type in each of the two experiments. The minimum number of cases required for a type was 10. The two–correlations method resulted in four easily distinguished types, while the basic method yielded 17 less distinguishable types. The classification of each map for 1961–62 is shown for each method of derivation in table 8. With the basic Lund method less than 0.3 percent of the cases were uncorrelated; however, over 53 percent of the sample maps were correlated to three or more types, and 85 percent to two or more. In the two–correlations experiment there was the problem of 18.5 percent of the sample being uncorrelated to any of the four types, but 71 percent of the sample maps were correlated to exactly one type, and at a higher level of correlation than in the first experiment.

The first four types of both experiments were very similar. The other types derived by the basic method were mostly minor variations of the four most common patterns and became increasingly difficult to distinguish.

41

Table 7. Number of Map Cases in Each Type in Each of the Two Experiments.

Type	Basic Lund Method	Two-Correlations Method	Two-Correlations Method With Four Gradients
A	351	305	288
B	225	127	123
C	210	96	100
D	147	21	28
E	121		26
F	97		16
G	70		
H	69		
I	39		
J	28		
K	25		
L	24		
M	24		
N	23		
O	18		
P	18		
O	12		

Table 8. Classification of Each Map for 1961-1962 According to, (a) the Basic Lund Derivation, (b) the Two-Correlations Method (No Gradients), and (c) the Two-Correlations Method With Gradients. (X - No Data Available, Blank - Untyped.)

(a)			(b)			(c)		
Dec.	Jan.	Feb.	Dec.	Jan.	Feb.	Dec.	Jan.	Feb.
CJ	X	ADH		X	AD	C	X	AD
J	ACEH	AD			AD		AD	AD
ABN		ACD	A	X	A	A	X	A
ACH	ABDH	BDI	A	B		AD		AB
ABD	ACH	ADEI	A	A		A	A	
BD	ABD	E	B	A		B	AB	E
B	BD	ACE	B	B	C	B	B	CE
BGKQ	BDG	CEM	B	B	C	B	B	C
BGKQ	BG	CEM		B	C	B	B	C
ACEF	H	X	A	B	X	A		X
BGK	ABD	X	B	D	X	B		X
BG	ABI	X	B	A	X	B	A	X
ABD	BK	X	B	B	X	B	B	X
BNO	ABH	X		AB	X		AB	X
AN	BI	X	A	B	X	A	B	X
ABHN	ABD	X	A	A	X	A	A	X
AF	AB	AI	A	A	A	A	A	A
A	X	AI	A	X		A	X	A
ACF	I		A			A		
X	O	Q	X			X		
AF		G	A			A		BF
ACH	G	BG	A		B	A	F	B
ACH	D	BKO	A	BD		A		
AC	ABD	GO	A	BD		A		
AB	ABDH	GKQ	A	A		A	A	
ABD	ABDH	GKQ	A	A		A	A	
ABD	ADH	BGK	A	A	B	A	A	B
AH	ADH	ABFIO	A	AD	A	A	AD	A
AD	AD		A	D		A	D	
ABD	DP		AB	D		AB	D	
D	AD		D	AD			AD	

43

Because the linear correlation coefficient is in reality the covariance of normalized variables,

$$r_{xy} = \frac{\sum(X_i - \bar{X})(Y_i - \bar{Y})}{\sqrt{\sum(X_i - \bar{X})^2 (Y_i - \bar{Y})^2}}$$

$$= \frac{\sum xy}{n\sigma_x\sigma_y}$$

$$= \frac{\sum z_x z_y}{n} \quad ,$$

where z_x and z_y are the normalized variables of X and Y respectively, maps with very different horizontal pressure or height gradients will be very highly correlated, by reason of the division by the standard deviations σ_x and σ_y, so long as the shape of their respective flows are similar.

Gradients tend to emphasize two features simultaneously, the overall strength of the flow and the sense of curvature in the pattern. The differences in curvature is seen by taking four gradients around the perimeter of the patterns shown in figure 18. The cyclonic pattern has strongest gradients on the north and east edges and weaker gradients on the south and west edges, while the anticyclonic pattern is just the opposite. Both patterns are basically NW flow. The gradients weight the correlation according to the strength and curvature of the flow; therefore, the larger the number of gradients used, the less weight is given to the basic pattern.

A third map typing was performed in which the number of grid points was reduced to 15, and four gradients were introduced, as shown in figure 19. Two correlations with the same values, 0.85 and 0.70, were used. The number of cases in each derived type is shown in table 7, where we see that, compared with the first two experiments, fewer cases fall into the most frequent types, and more cases are in the less frequent types. Figure 20 shows the six types. The percentage of uncorrelated maps was reduced to 16 percent and the number of two-type maps was increased to 13.8 percent as compared with 18.5 percent and 10.5 percent respectively by the two-correlations method alone.

Both the basic two-correlation and two-correlation-with-gradients map types are being tested for usefulness in predicting surface winds at the NRTS. The results will be presented in the next report.

44

Figure 17. The 29 NMC grid points used for deriving 700-mb map types in experiments one and two.

Figure 18. Two northwest flow patterns. a) cyclonic in solid line, b) anti-cyclonic in dashed line. Four gradients are measured along the lines AB, BC, CD and DA.

45
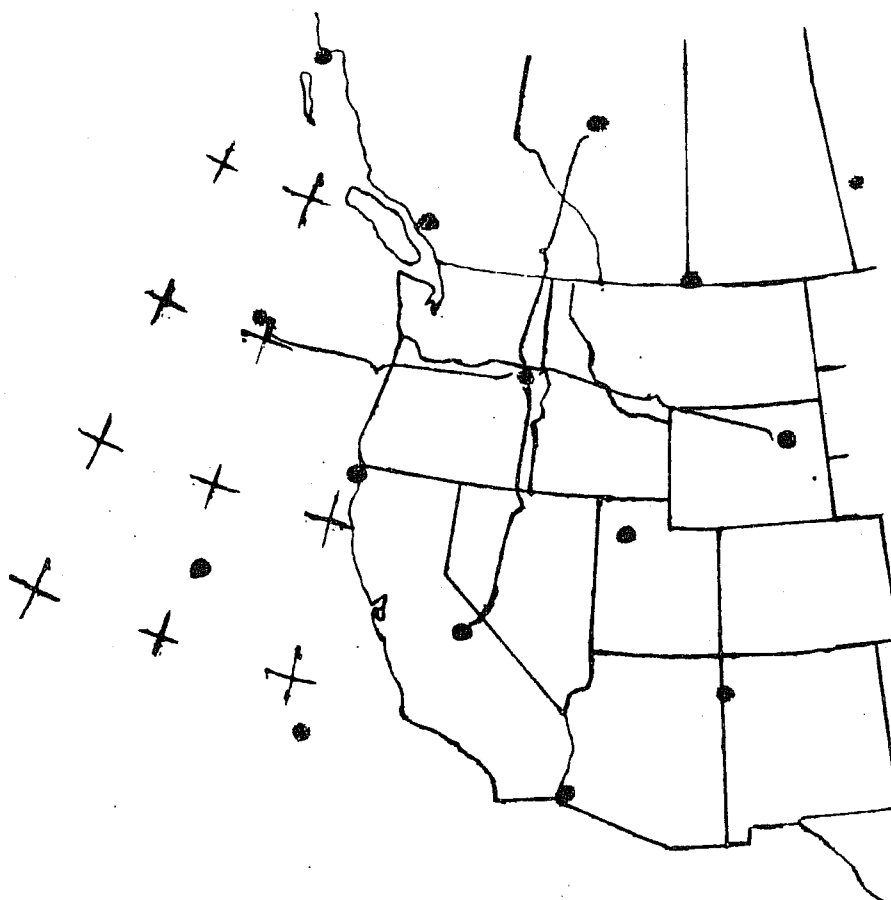
Figure 19. The 15 NMC grid points used for deriving 700-mb map types in experiment three. The four gradients used in the derivation are indicated.

2.5 Forecast Verification

The results of verification of temperature, precipitation, and wind forecast for February 1965 through June 1969 are presented briefly in tables 9, 10, and 11. The Idaho FRO operates only 8 hours per day, 5 days a week. The first forecast for the day is made at 0900 MST for the 12-hour period already begun, namely 0800 MST to 2000 MST, after a review of the current and previous day's facsimile charts. The second forecast of the day is made at 1500 MST for the next 12-hour period from 2000 MST to 0800 MST following a brief review of the day's facsimile charts, the forecaster having been on another assignment during the day. Winds are verified on the maximum average hourly wind for a 6-hour period beginning at either noon or midnight. Forecasts for the station were terminated as of January 1, 1970; forecasts for test operations are still being made on request.
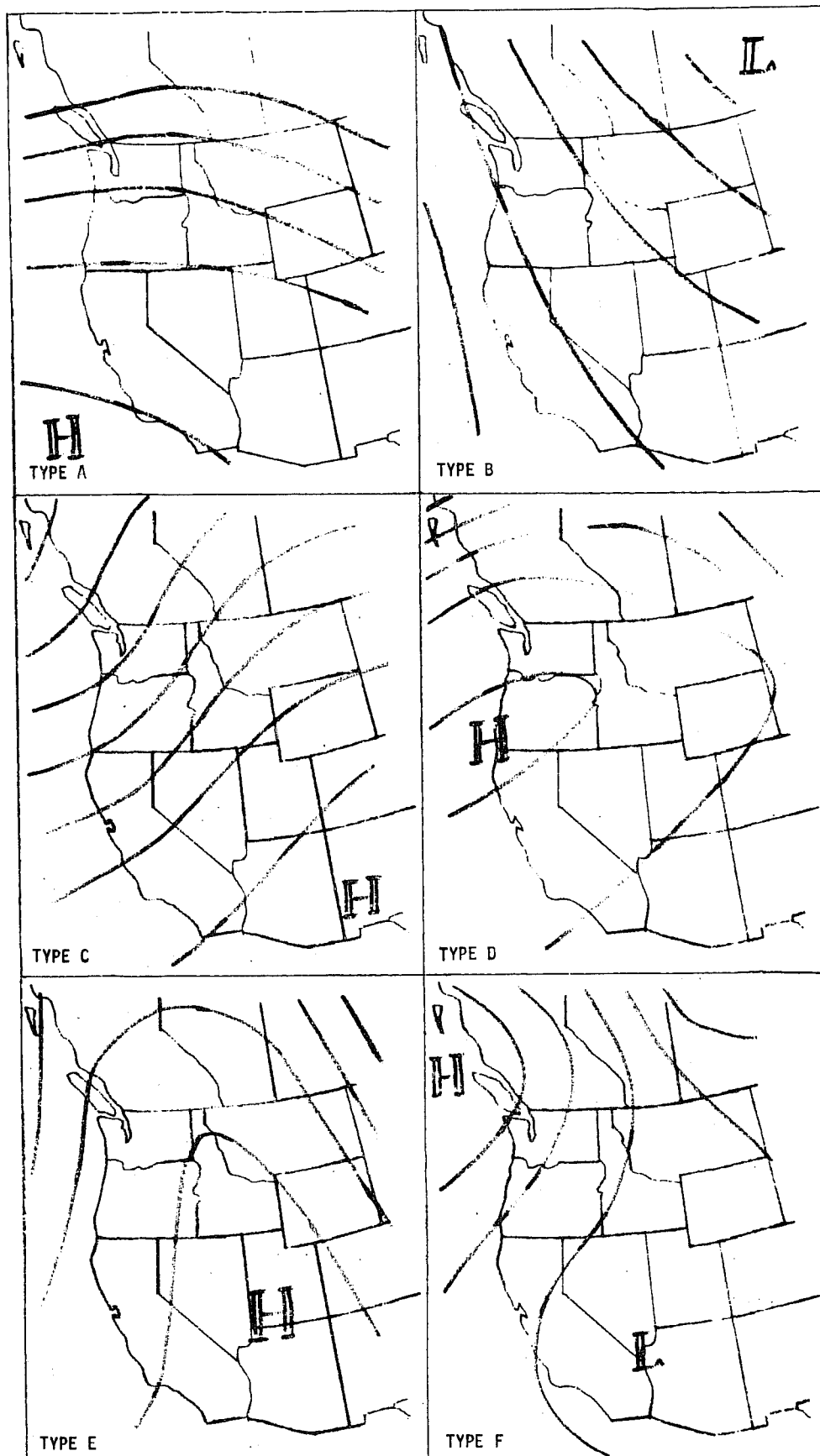
Figure 20.   The six 700-mb map types derived by the two-correlations-with-gradients method with significant correlationd equal to 0.85 and 0.70.

Table 9. Maximum and Minimum Temperature Forecast Verification (a) Average Error °F; (b) Percentage Cases With Errors ≤ 3°F.

| | 0900 MST Forecasts | | | 1500 MST Forecasts | | |
	Today	Tonight	Tomorrow	Tonight	Tomorrow	Tomorrow Night
(a)						
Winter	3.4	6.9	4.4	6.3	4.1	8.2
Spring	2.8	4.9	4.6	4.4	3.8	5.5
Summer	2.4	4.1	4.8	4.0	4.0	4.8
Autumn	3.0	5.2	4.4	4.6	4.0	6.1
(b)						
Winter	61%	36%	47%	37%	53%	26%
Spring	70%	41%	48%	47%	53%	39%
Summer	77%	54%	50%	53%	59%	46%
Autumn	60%	44%	50%	47%	54%	37%

Table 10. Percentage of Forecasts in Which Occurrence or Nonoccurrance of Measurable Precipitation Is Correctly Forecast.

| | 0900 MST Forecasts | | | 1500 MST Forecasts | | |
	Today	Tonight	Tomorrow	Tonight	Tomorrow	Tomorrow Night
Winter	84%	75%	72%	78%	76%	73%
Spring	81%	84%	78%	84%	78%	82%
Summer	82%	82%	84%	80%	80%	80%
Autumn	87%	82%	83%	83%	82%	87%

Table 11. Wind Forecast Verification. (a) Average Vector Error in mph;
(b) Percentage of Cases in Which Forecast Direction Missed by
More Than 90°.

| | 0900 MST Forecasts | | | 1500 MST Forecasts | | |
	Today	Tonight	Tomorrow	Tonight	Tomorrow	Tomorrow Night
(a)						
Winter	8.8	9.0	11.6	8.7	11.2	9.9
Spring	8.6	9.5	12.1	9.2	11.6	9.4
Summer	9.4	9.2	10.9	9.0	10.9	9.6
Autumn	8.1	9.7	11.1	9.0	9.9	10.1
(b)						
Winter	26%	42%	37%	41%	34%	49%
Spring	14%	47%	25%	45%	23%	43%
Summer	17%	49%	22%	45%	25%	51%
Autumn	18%	51%	29%	47%	27%	50%

2.6 Turbulent Wind Velocity Components From Hot Wire Arrays

Since the cooling of a hot wire in a moving air stream is a measure of the component of the wind velocity normal to the wire when the angle between the airstream vector and the wire is large ($> 20°$), arrays of hot wires can theoretically be used to determine the magnitude of the total velocity vector $|V|$ and its components at a point in space. An orthogonal array of three hot wires should make it possible to determine $|V|$ and the magnitudes of the velocity components with a system of linear equations in the squares of the components (fig. 21).

To determine the signs of the individual components a nonorthogonal array has to be used. Theoretically, four wires can be arrayed to determine component magnitudes and signs within a spherical octant, and five wires can be used to resolve component magnitudes and signs within a hemisphere. A typical array of five hot wires and their equations are shown in figure 22. This array provides

49

Schematic of Wire Array:

Schematic of Wire Array:
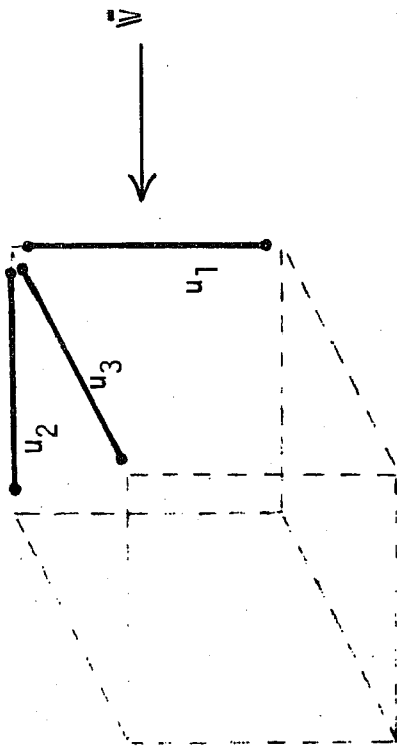
Equations:

$$u_1^2 = u^2 + v^2$$

$$u_2^2 = v^2 + w^2$$

$$u_3^2 = u^2 + w^2$$

Solutions

$$u^2 = \frac{1}{2}(u_1^2 - u_2^2 + u_3^2)$$

$$v^2 = \frac{1}{2}(u_1^2 + u_2^2 - u_3^2)$$

$$w^2 = \frac{1}{2}(-u_1^2 + u_2^2 + u_3^2)$$

$$|V|^2 = u^2 + v^2 + w^2 = \frac{1}{2}(u_1^2 + u_2^2 + u_3^2)$$

Equations:

$$u_1^2 = v^2 + w^2$$

$$u_2^2 = \frac{1}{2}(u + w)^2 + v^2$$

$$u_3^2 = \frac{1}{2}(u - w)^2 + v^2$$

$$u_4^2 = \frac{1}{2}(u + v)^2 + w^2$$

$$u_5^2 = \frac{1}{2}(u - v)^2 + w^2$$

$$|V|^2 = \frac{1}{2}(u_2^2 + u_3^2 + u_4^2 + u_5^2 - u_1^2)$$

Figure 21. Orthogonal array of three hot wires and equations.

Figure 22. Non-orthogonal array of five hot wires and equations.

a set of five equations with three unknowns, and a unique solution should exist. A computer program has been written to solve all possible sets of three equations for u, v, and w by the Newton-Raphson method for solution of simultaneous nonlinear equations. The results show that u, v, and w are different by about 5 to 10 percent for each set of equations. One of the factors contributing to this difference is a dislocation of the wires in the array thus changing the angles between the various wires. An improvement in the instrumentation is now underway.

2.7 Environmental Chamber

The environmental chamber is in the process of being modified to simulate atmospheric conditions within 1 m above a grass canopy. An initial survey of mean wind velocity at 1-ft intervals throughout the working section, which is 3 ft wide, 4 ft high, and 12 ft long, showed that the velocity gradients were not uniform. In the vertical direction, the velocity profiles were nearly logarithmic because of suppression of the air flow at the lower levels by baffles upwind of the working section. In the crosswind horizontal direction, the velocity distribution was skewed, showing the effect of right angle bends in the duct upstream and downstream from the working section.

To simulate atmospheric conditions, a uniform velocity in the crosswind horizontal direction and a nondeveloping logarithmic velocity profile in the vertical direction is desired. Flow straighteners in the form of thin sheet aluminum alloy, 1/4-in. honeycombs 6 in. deep were installed immediately upstream and downstream from the working section. This produced laminar flow, maintained a nondeveloping nearly logarithmic velocity profile in the vertical direction, and produced a nearly uniform velocity through any horizontal crosswind section.

The next step in the atmospheric simulation process was the development of turbulence. First, the floor of the working section was covered with grass in 10 in. x 10 in. flats. The flats were 5 in. deep, and the average grass height was 7 in., which lowers the across-flow area from 12 ft^2 to 9 ft^2. Theoretical calculations showed that the turbulent boundary layer developed by the grass surface should be 5 in. deep after traversing a 10-ft fetch. Turbulence measurements from hot wires were made 1, 12 and 24 in. above the grass. The results verified the theoretical calculation in that the highest turbulence intensity was found at the 1-in. sampling level, but the shape of the spectra of turbulence was quite different from those computed from atmospheric data. Environmental chamber vibration was transmitted to the hot wires during the runs and may have had some influence on the shape of the spectra.

Turbulence generators in the form of 1 ft x 3 ft plates of 1/8 in. Plexiglas measuring 1 ft along the flow and oriented in a horizontal position with lateral strips of 1/8 in. Plexiglas 7/8 in. high near the upstream and downstream edges were installed upwind of the working section of the chamber.

These turbulence generator plates were spaced logarithmically to see the character of the turbulence generated artificially. Two 10-min analog runs of the output from vertically oriented hot wires 9 ft downstream from the turbulence generators were made, 6 and 18 in. above the bottom of the chamber, one for the highest and the other for the lowest chamber flow rate. The analog wires were digitized at 40 samples/sec and average spectra from five sets of 4096 data points were computed (fig. 23). The ordinate values in the spectral plots represent normalized energy. Eddy kinetic energy dissipation in accordance with the $-5/3$ law was generated for frequencies greater than 1 Hz. Since the energy distribution was nearly uniform at lower frequencies, we conclude that the artificial turbulence produced by the generators is reasonably realistic.

Turbulence measurements will soon be made over real grass with the turbulence generator plates to see if atmospheric turbulence conditions can be simulated in the chamber.

2.8 Hemispheric Dispersion

A method has been proposed for investigating the dispersive nature of large-scale wave motion over the northern hemisphere (ESSA Tech. Memo. ERLTM-ARL 9, 1968). Basically it consists of releasing hypothetical particles equally spaced around a latitude circle, advecting them with historical streamfunction data, and computing the variance of their north-south distances from the release latitude. At the time the report cited above was written, two items required further attention before computations could be made for more than a week of advection time. First, various methods of time interpolation between the 0000Z and 1200Z map times were being investigated, and, second, an acceptable method of handling the problem of particles leaving the computational grid was being sought.

In investigating time interpolation techniques, we decided that linear interpolation between maps might be too coarse for calculations for long periods. Two other methods were tested. The first was a polynomial interpolation that has been used before by Mesinger (1965) with three maps; we used four. The second method tested, also with four maps, was a third order spline fit. Since spline interpolation is theoretically smoother and its computation is more economical, it was chosen over polynomial interpolation. In a comparison of the dispersion results for 20 days using the linear and spline time interpolations, we found that the curves followed each other quite closely for about 8 days, diverged to a separation of more than 30 percent at 10 days, converged again at 13 days, and were reasonably close for the rest of the period. Since the proposed tests were for 30-day periods, the spline interpolation was selected for use in these computations.

The problem of handling particles that leave the computational grid is fairly serious in latitudinal variance calculations, because as a particle reaches the edge of the grid its contribution to the variance is quite large. However, the flow in the equatorial latitudes is such that the north-south motion of particles in this region is small compared with that at the temperate
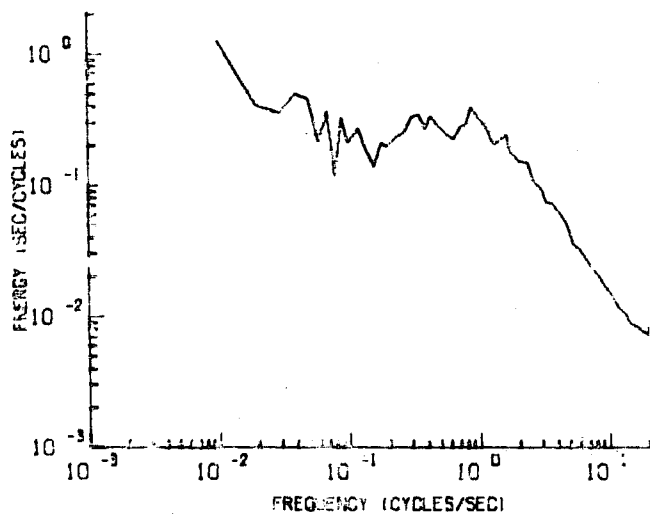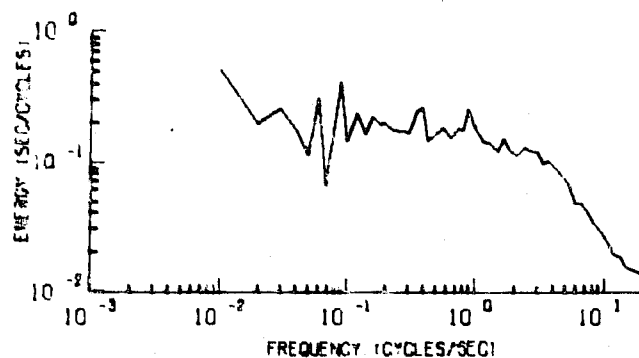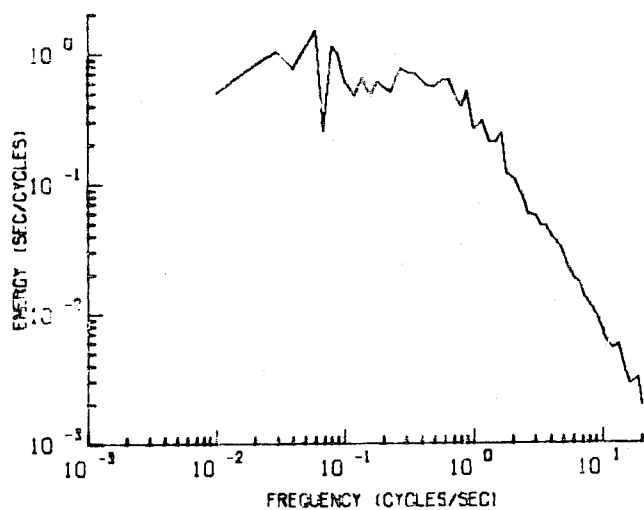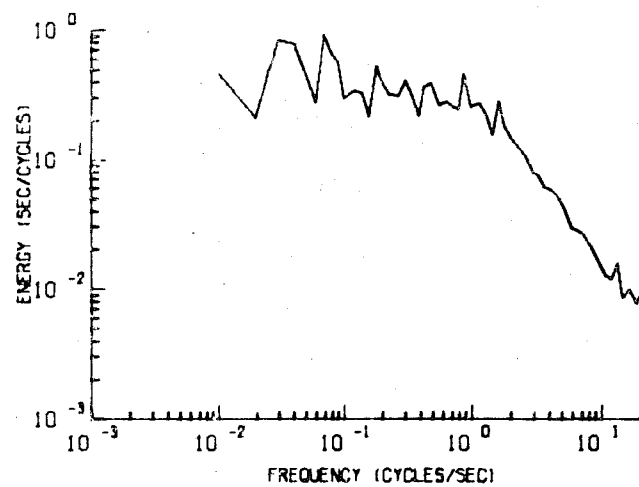
Figure 23. Sample turbulent energy spectra from the environmental chamber.

and northern latitudes. The technique decided upon is similar to one used before (J.K. Angell, 1969, personal communication). First an effective latitude is computed from the standard deviation of particle position as follows:

$$\phi_e(t) - \phi_r = \frac{\sigma_y(t)}{R} \qquad (4)$$

where ϕ_r is the latitude of release, $\sigma_y(t)$ is the standard deviation of north-south distances of the particles from the latitude of release, and R is the radius of the earth. The north-south positions of particles off the grid at time t are then obtained by adding to them the quantity $(\phi_e(t-\Delta t) - \phi_e(t-2\Delta t))R$. The positions of all the particles are then used to calculate the variance $D_L(t)$ of north-south distances from the release latitude.

The experiment reported here consisted of five separate 500-mb releases of 72 particles, with a 5^0 separation around the latitude circle of 52.5°N. These releases were 6 days apart during December 1969, and each set of particles was followed for 30 days. Plots of $D_L(t)$, which is a measure of latitudinal dispersion, are shown in figures 24a-e. The dashed lines show the contribution to $D_L(t)$ from particles that are off the computational grid.

A characteristic common to all the releases was a rapid rise in $D_L(t)$ for the first 2 to 4 days and then a change to a more gradual increase with time. L. Machta (1969, personal communication) has suggested that this initial rapid spread of particles away from the release latitude cannot be considered true dispersion because the same phenomenon occurs when particles are being advected by non-dispersive flow containing sinusoidal wave motion. However, if we consider the behavior of $D_L(t)$ for all five releases during the period between 6 and 30 days after release, we find that linear regression lines seem to fit reasonably well. We can estimate the magnitude of the lateral eddy diffusivity from the expression $K = D_L(t)/2t$. This means that the magnitude of K for each release would be one-half the value of the slope of each regression line. An estimate of K has been made previously (Angell and Hass, 1966) with a smaller sample and with the release points contained in the latitude band $55^0 - 65^0$ N. For our estimate, we used the value of the lateral variance 15 days after release and found that K had a value of 1.8 x 10^{10} cm^2 sec^{-1} for the winter of 1962. Values of K estimated separately from the slopes of the regression lines and 15-day values of $D_L(t)$ for the five releases are shown in table 12. The average value of K for the 15-day estimate is about the same as that obtained by Angell and Hass, but the average estimate from the regression lines is only about half as large. The reason may be attributable to the rapid rise in lateral variance during the first few days. Angell and Hass found the value of K for a 60-day travel time to be about half that for the 15-day travel time. They suggest that the usual tendency for the lateral eddy diffusivity to increase with an increase in travel time was being offset by the latitudinal bounds on the data. More plausible, in view of $D_L(t)$ as

(a) 500 MB 52.5 N 0000Z 12/02/63 DT=1 HRS, TIME INTP. - SPLINE
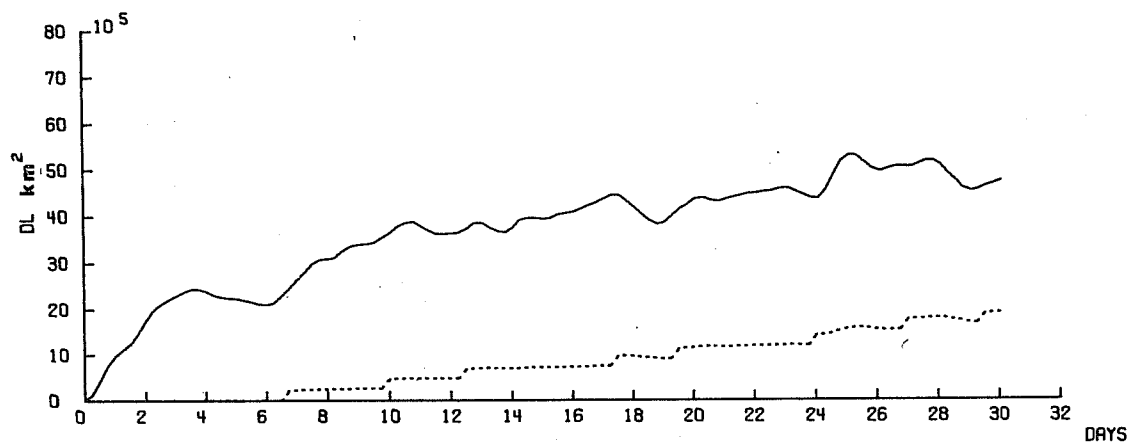
(b) 500 MB 52.5 N 0000Z 12/08/63 DT=1 HRS, TIME INTP. - SPLINE
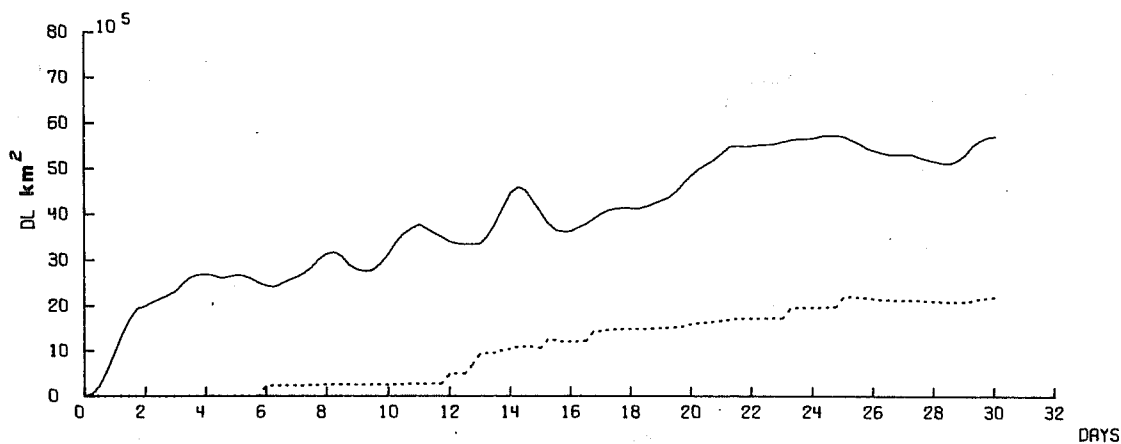
(c) 500 MB 52.5 N 0000Z 12/14/63 DT=1 HRS, TIME INTP. - SPLINE

Figure 24. Hemispheric dispersion, $D_L(t)$, of 72 particles released from equally spaced positions around latitude 52.5°N on the 500 mb-surface. The dashed lines represent the contribution to $D_L(t)$ from particles which have left the computational grid.

55

(d) 500 MB 52.5 N 0000Z 12/20/63 DT=1 HRS, TIME INTP. - SPLINE

(e) 500 MB 52.5 N 0000Z 12/26/63 DT=1 HRS, TIME INTP. - SPLINE

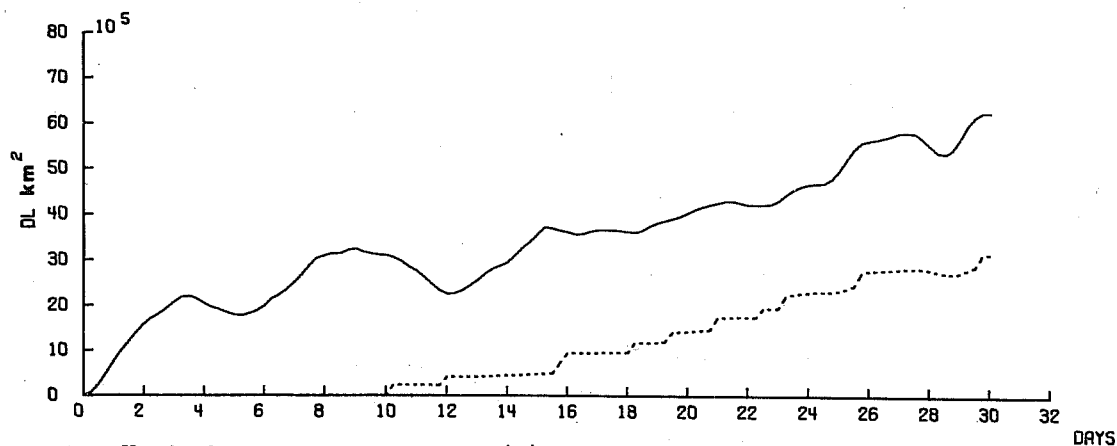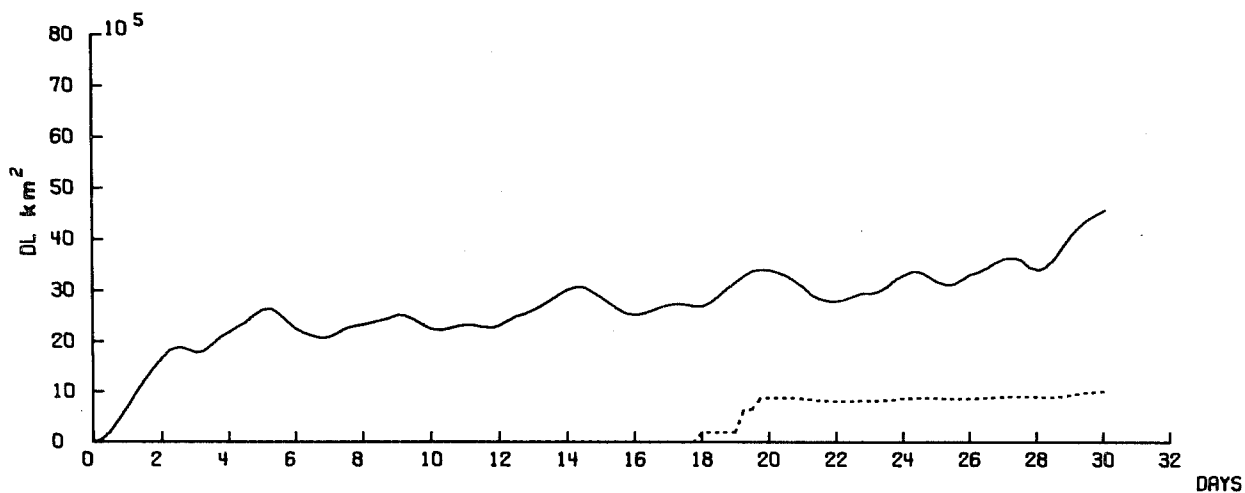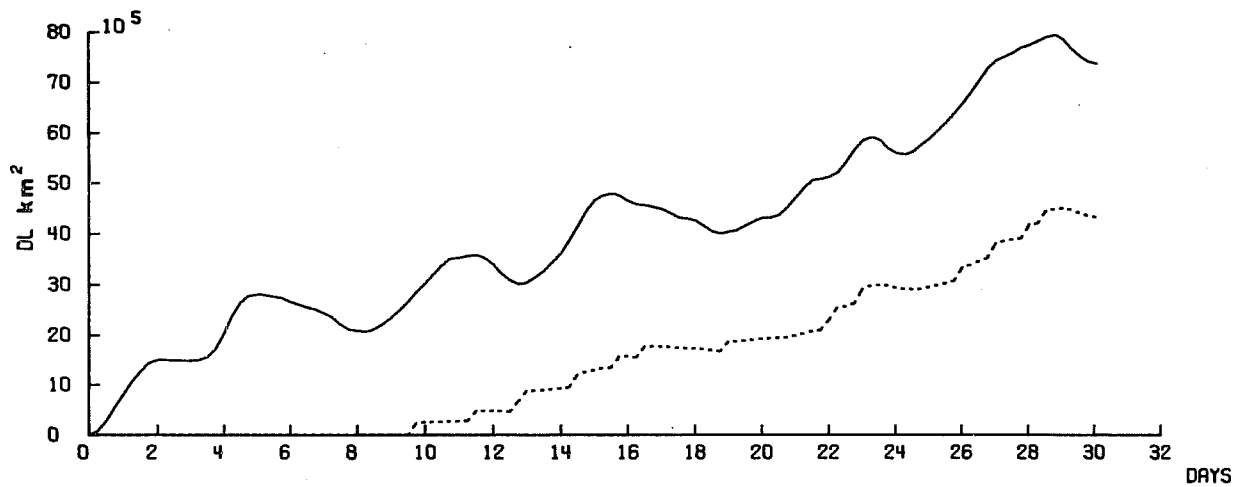Figure 24. Hemispheric dispersion (continued).

56

seen in figures 24a through e is that K does not change with time if the
first 3 to 5 days of travel time are excluded from the calculations. The
rapid rise of $D_T(t)$ during this period and the oscillations, with 3- to 6-
day periods which occur from 6 to 30 days, can probably be attributed
to the nondispersive part of the wave motion in the flow. The latitudinal
bounds on the data and the finite number of particles in the release do seem
to affect the magnitude of the slope of the regression line for each release,
as evidenced by the variation in the estimates of K for each release and the
variation in the number of particles that left the grid.

Table 12. Estimates of Lateral Eddy Diffusivity.

| Release Date | $K \times 10^{10}$ cm^2 sec^{-1} | |
	t = 15 Days	Regression
12/02/63	1.6	0.4
12/08/63	1.6	0.8
12/14/63	1.4	0.9
12/20/63	1.1	0.4
12/26/63	1.7	1.4
Average	1.5	0.8

2.9 Diffusion and Deposition Studies

The validity of using a deposition and diffusion climatology derived
for uranine dye in estimating the deposition and diffusion of molecular
iodine has been tested over the past 2 years. A series of four diffusion
experiments were conducted between November 1967 and October 1969. A
simultaneous release of molecular iodine and uranine dye (CDT I) was made
in November 1967 (ESSA Tech. Memo. ERLTM-ARL 5, 1968); two tracer diffusion
experiments (CDT II & III) were perofrmed in May 1968 (ESSA Tech. Memo.
ERLTM-ARL 14, 1969), in which a methyl iodide and uranine dye paired release
(CDT II) was followed by a methyl iodide and molecular iodine paired release
(CDT III) about 2 hours later; a repeat paired release (CDT IV) of methyl
iodide and molecular iodine in a test during October 1969. All tests were
conducted under lapse conditions. The results are presented below.

The lateral diffusion values, σ_y, at various downwind distances are
listed in table 13. The σ_y values for molecular iodine (CDT IV) were greater
than those for methyl iodide. The σ_y values for uranine dye (CDT II) were
less than for methyl iodide. The ratio between methyl iodide normalized σ_y
values for uranine dye and molecular iodine indicates measured uranine dye
lateral spreading is about 75 percent greater than molecular iodine under the
conditions of these tests.

57

Table 13. Lateral Diffusion, σ_y^{-} (in Meters).

Distance	CDT IV			CDT II Ratio Dye/Methyl	Ratio Dye/Molecular
	Methyl	Molecular	Ratio		
100	18.7	25.7	1.37	0.83	0.606
200	32.3	36.2	1.12	0.96	0.857
400	54.1	67.8	1.25	0.96	0.768
800	110.3	125.2	1.14	0.92	0.807
1600	192.8	221.8	1.15	0.65	0.565
3200	364.0	599.3	1.65	-	-

Mean dye to molecular ratio: 0.72

Table 14. Ratios of CIC/Q Values.

Distance	CDT IV Methyl/Molecular	CDT II Methyl/Dye	Ratio Dye/Molecular
50	1.6	2.8	0.571
100	1.1	3.4	0.324
200	1.8	4.6	0.391
400	1.5	4.5	0.333
800	2.0	4.6	0.435
1600	1.8	4.6	0.391

Mean dye to molecular ratio: 0.41

The ratios between source strength normalized crosswind integrated concentrations (CIC/Q) are listed in table 14. The ratio values for CDT II show a smooth, systematic trend with downwind distance. The uranine dye plume depletion stabilized at about 200 m, at where about 80 percent of the plume mass was apparently deposited on the ground surface. For molecular iodine (from the CDT IV measurements) the ratio values were not as smooth, although a two-point running mean of the CIC/Q for dye to molecular iodine shows no particular dependence upon distance. An average CIC/Q ratio of 0.4 for dye to molecular iodine appears reasonably descriptive for distances within 1600 m downwind from the release point. Uranine dye samples beyond this distance were below background detectability limits, and no comparison was made for the 3200-m sampling arc.

Tower-collected sample values of $\chi \bar{u}/Q$ are listed in table 15. The ratio of normalized total effluent mass, $\chi \bar{u}/Q$, collected by all samplers on four 100-ft towers 385 m downwind is 1.443 (see table 15). This ratio value is 96 percent of the 400-m arc ratio of CIC/Q values. This agreement indicates that there is no significant difference in the upward or vertical diffusion of methyl iodide and molecular iodine. The conclusion again, as for CDT II, is that ground deposition is producing the bulk of differences observed in tracer diffusion statistics.

In the belief that ground deposition probably produces the major differences in diffusion statistics, nearly 100 carbon fallout plates were placed on the diffusion grid. The deposition on these plates was used to estimate the total integrated deposition of molecular iodine, to calculate deposition velocities, and to further examine the vertical mass flux differences implied by the CIC/Q ratios and tower samples. Table 16 lists the crosswind integrated deposition rate (CID), the crosswind integrated concentration (CIC), and the calculated deposition velocities (Vd). The units are Ci/m/sec, Ci/m^2, and cm/sec, respectively.

The deposition velocities at 25- and 50-m arcs tend to be large because the limited number of air samples poorly represented the CIC values. Concentration values, and therefore CIC values, at distances less than 200 m downwind are systematically underestimated because the filter collection efficiencies, relative to one another, change according to effluent loading rate. The mean deposition velocity for molecular iodine on all arcs is 1.24 cm/sec. Excluding values at less than 100 m downwind, the mean deposition velocity is 0.89 cm/sec. Measurements from CERT testings at the NRTS yielded a mean deposition velocity for carbon plates of about 0.8 cm/sec.

Carbon fallout plate estimates of total integrated deposition and the resulting fractional plume depletion are shown in table 17, which indicates that approximately 10 percent of the molecular iodine was deposited on the grid downwind to 3200 m. The corresponding estimated plume depletion based on CIC ratios was 50 percent of the total effluent mass released. The comparisons between CIC/Q ratios is believed more representative. Fallout plate sampling from CERT tests have shown considerable variation between carbon and soil-vegetation deposition.

Table 15. Tower Values of $\chi\bar{u}/Q$* for CDT IV.

Height

Tower	Sfc. M.I.	Sfc. MOL. I	20' M.I.	20' MOL. I	40' M.I.	40' MOL. I	60' M.I.	60' MOL. I	80' M.I.	80' MOL. I	100' M.I.	100' MOL. I
1	36.95	20.39	38.06	26.84	36.66	20.77	23.87	17.80	12.20	14.19	10.52	10.13
2	26.64	14.95	23.85	14.25	23.15	15.32	31.62	13.65	13.93	12.12	15.33	11.02
3	6.11	5.69	4.63	6.00	4.94	6.09	3.95	3.81	3.16	3.34	3.14	2.84
4	0.13	0.39	0.19	0.46	0.42	0.73	-	-	0.28	0.37	0.27	0.45

Sum of all methyl iodide $x\bar{u}/Q$ = 320.00

Sum of all molecular iodine $x\bar{u}/Q$ = 221.69

Ratio total methyl/total molecular = 1.443

* All values of $\chi\bar{u}/Q$ x 10^{-5}

60

Table 16. Carbon Fallout Plate Deposition and Deposition Velocities.

Arc	CID(Ci/m/sec)	CIC(Ci/m^2)	$\overline{Vd}$(cm/sec)
25	1.4437	76.50	1.89
50	1.1118	40.78	2.73
100	0.5024	61.72	0.81
200	0.2123	20.24	1.05
400	0.09677	12.64	0.77
800	0.03603	4.827	0.75
1600	0.02034	1.442	1.41
3200	0.006667	1.275	1.41

Mean V_d all arcs: 1.24

Mean V_d 100-3200 m: 0.89

Table 17. Carbon Plate Estimates of Iodine-131 Deposition and Plume Depletion.

Arc (meters)	Crosswind (Ci/m)	Arc to Arc TID (Ci)	Source Fraction Remaining Airborne
6	935.8	8462.8	.998
12	1885.2	31396.4	.992
25	2945.1	65163.0	.979
50	2268.0	82318.0	.962
100	1024.8	72886.5	.947
200	433.0	63035.0	.934
400	197.4	54180.0	.923
800	73.5	46008.0	.914
1600	41.5	44088.0	.905
3200	13.62		

Total Grid Deposition = 467569. μ Ci

Total Plume Depletion Fraction to 1600 m = 0.086   Deposition Measurements

Total Plume Depletion Fraction to 1600 m = 0.45   Ratio of CIC $\bar{u}$/Q Measurements

The absolute comparisons between dye and molecular iodine must be tempered by the following considerations. The uranine dye solution dispensed during CDT II was about nine times more concentrated than solutions normally used for field diffusion studies at the NRTS. All other factors being nearly equal, the mean dye particle radii were probably twice as large as normal. The effect of doubling particle radii is an increase in gravitational settling rate by two to four times. This gravitational settling speed is still two orders of magnitude smaller than dry deposition values found by Islitzer and Dumbauld (1963).

The broad conclusions concerning the use of uranine dye diffusion statistics to describe molecular iodine behavior are the following:

(a) A substantial difference in dry deposition velocities exist between the two substances and reducing the dispersed dye particle sizes would probably result in little improvement.

(b) Iodine concentration may be underestimated from a uranine dye based diffusion climatology. The differences in lateral spread and surface deposition rates attempt to compensate each other, but deposition characteristics dominate the process and may yield underestimated plume concentrations.

Because this field diffusion test series required many man-hours, only four have been conducted. The absolute values of dye comparisons to molecular iodine lack a broad statistical basis. It is believed that the mass balance approach (CIC/Q ratios) in estimating deposition is more reliable than spot ground sampling using carbon plates.

3. REFERENCES

Angell, J. K. and W. A. Hass, (1966), Effect of clustering upon a 500 mb horizontal sounding system. Monthly Weather Rev. 94, No. 2, 151-165.

Boyton, H. W., (1969), Project Clambake surface wind analysis at Palestine, Texas, NCAR Tech. Note 33, 38 pp.

Dickson, C. R. (Ed.), (1967), Meteorology for the Loss-of-Fluid-Test Reactor, Progress Report, IDO-12059, 55 pp.

ESSA Tech. Memo. Atmospheric transport and diffusion in the planetary boundary layer. Air Resources Laboratories Semiannual Research Program Review for the Division of Reactor Development and Technology, USAEC, ERLTM-ARL 5 (1968), 60 pp; ERLTM-ARL 9 (1968), 60 pp; ERLTM-ARL 14 (1969), 44 pp; ERLTM-ARL 17 (1970), 46 pp.

Islitzer, N. F. and R. K. Dumbauld (1963), Atmospheric diffusion-deposition studies over flat terrain. Intern. J. Air Water Pollution 7, 999-1022.

Mesinger, F., (1965), Behavior of a very large number of constant-volume trajectories, J. Atmospheric Sci. 22, No. 5.

Priestley, C. H. B. and W. C. Swinbank, 1947), Vertical transport of heat by turbulence in the atmosphere, Proc. Roy. Soc., A , 189, 543-561.

Saltzman, B., (1959), On the maintenance of the large-scale quasi-permanent disturbances in the atmosphere, Tellus 11, No. 4, 425-431.

Slade, D. H., (1969), Wind measurements on a tall tower in rough and inhomogeneous terrain, J. Appl. Meteorol. 8, No. 2, 293-297.

4. REVIEW OF REACTOR SAFETY ANALYSIS REPORTS

The Air Resources Laboratories in Silver Spring, Maryland, and the Field Office in Idaho have continued to take an active part in the review of reactor safety analysis reports as well as consultations with regard to the preparation of the reports. In addition, written comments have been prepared for the Division of Reactor Licensing through the Division of Reactor Development and Technology.

1. Enrico Fermi Atomic Power Plant Unit 2, Detroit Edison Company. Preliminary Safety Analysis Report, Volumes I through V, dated April 29, 1969.

2. Turkey Point Units 3 and 4, Florida Power and Light Company Final Safety Analysis Report, Volumes I, II, and III dated May 12, 1969.

3. Midland Plant Units 1 and 2, Consumers Power Company Preliminary Safety Analysis Report, Amendment No. 2, dated June 5, 1969.

4. Indian Point Nuclear Units 4 and 5, Consolidated Edison Company of New York Preliminary Safety Analysis Report, Volumes I through V, dated June 3, 1969.

5. Millstone Nuclear Power Station Unit 2, The Connecticut Light and Power Company et al. Preliminary Safety Analysis Report, Volumes I and II, dated February 28, 1969.

6. American Electric Power Service Corporation, Re: Docket Nos. 50-315, 50-316, Donald C. Cook Nuclear Plant, Report entitled "Tornado and Missile Considerations," dated June 1969.

7. Diablo Canyon Site Nuclear Unit 2, Pacific Gas and Electric Company Preliminary Safety Analysis Report, Volumes I, II, III, dated June 28, 1968 and Amendments I through IV.

8. Trojan Nuclear Plant, Portland General Electric Company Preliminary Safety Analysis Report, Volumes I, II, and III, dated June 25, 1969.

9. Omega West Reactor, Los Alamos Scientific Laboratory Revised Safety Analysis, dated July 15, 1969.

10. Beaver Valley Power Station, Duquesne Light Company Preliminary Safety Analysis Report, Amendment IV, dated September 3, 1969.

11. Davis-Besse Nuclear Power Station, Toledo Edison Company Preliminary Safety Analysis Report, Volumes I, II, and III, dated August 1, 1969.

12. Diablo Canyon Site Nuclear Unit 2, Pacific Gas and Electric Company Preliminary Safety Analysis Report, Amendment VI, dated September 25, 1969.

13. Seala Nuclear Plant, Unit I, Alabama Power Company Preliminary Safety Analysis Report, Volumes I through IV, dated October 15, 1969.

14. Shoreham Nuclear Power Station, Long Island Lighting Company Preliminary Safety Analysis Report, Amendment VII, dated August 22, 1969.

15. James A. Fitzpatrick Nuclear Power Plant, Power Authority of the State New York Preliminary Safety Analysis Report, Amendment No. VIII, dated November 5, 1969.

16. Sequoyah Nuclear Plant, Tennessee Valley Authority Preliminary Safety Analysis Report, Amendment No. I, dated February 6, 1969.

17. Comments on letter from Vice President, Consolidated Edison Company of New York, Inc. dated December 2, 1969, re: Lower New York Bay and Fort Slocum Sites.

5. PUBLICATIONS

1. Angell, J. K., D. H. Pack and N. Delver, "Brunt-Vaisala Oscillations in the Planetary Boundary Layer." J. of Atmospheric Sci. 26, No. 6, 1245-1252, November 1969.

2. Hoecker, W. H. and J. K. Angell, "Effect of a Sudden Change in Terrain Height on the Three-Dimensional Low-Level Air Flow as Estimated by Tetroon Flights." Monthly Weather Rev. 97, No. 12 845-849, December 1969.

3. Slade, D. H., "Low Turbulence Flow in the Planetary Boundary Layer and Its Relation to Certain Air Pollution Problems." J. Appl. Meteorol. 8, No. 4, 514-522, August 1969.

4. Van der Hoven, I. and W. P. Gammill, "A Survey of Programs for Radiological-Dose Computation." Nuclear Safety, 10, No. 6, 513-521, Nov - Dec 1969.

6. LABORATORY PERSONNEL

Silver Spring, Maryland

David H. Slade, meteorologist, returned to ESSA on November 3, 1969 from temporary duty with the Fallout Studies Branch, U. S. Atomic Energy Commission, Germantown, Maryland.

Idaho Falls, Idaho

Dr. Gale Biggs and Mr. Archie Morgan of Iowa State University were visiting scientists during July collecting turbulence data using hot wire anemometers.

Earl H. Markee, meteorologist, was awarded an M.S. degree in Meteorology by the University of Utah on August 16, 1969.

Regina Young and Hal Shearer ended their summer employment as students on August 22, 1969 in preparation for beginning college studies in September.